Pergamon

Geochimica et Cosmochimica Acta, Vol. 68, No. 20, pp. 4267-4284, 2004

0016-7037/04 $30.00 + .00

doi:10.1016/j.gca.2004.03.014

Experimental constraints on crystallization differentiation in a deep magma ocean

M. J. WALTER,[1,*,†] E. NAKAMURA,[1] R. G. TRØNNES,[2] and D. J. FROST[3]

[1]Institute for Study of the Earth's Interior, Okayama Univ., Misasa, Tottori-ken 682-01, Japan
[2]Nordic Volcanological Institute, University of Iceland, Natural Sciences Building, IS-101 Reykjavík, Iceland
[3]Bayerisches Geoinstitut, Universität Bayreuth, D-95447 Bayreuth, Germany

(*Received August* 12, 2003; *accepted in revised form March* 11, 2004)

Abstract—Major and trace element mineral/melt partition coefficients are presented for phases on the liquidus of fertile peridotite at 23–23.5 GPa and 2300 °C. Partitioning models, based on lattice-strain theory, are developed for cations in the '8-fold' sites of majorite and Mg-perovskite. Composition-dependant partitioning models are made for cations in the 12-fold site of Ca-perovskite based on previously published data. $D^{min/melt}$ is extremely variable for many elements in Ca-perovskite and highly correlated with certain melt compositional parameters (e.g. CaO and Al_2O_3 contents). The 8-fold sites in Mg-perovskite and majorite generally have ideal site radii between 0.8 and 0.9 Å for trivalent cations, such that among rare-earth-elements (REE) $D^{min/melt}$ is maximum for Lu. Lighter REE become increasingly incompatible with increasing ionic radii. The 12-fold site in Ca-perovskite is larger and has an ideal trivalent site radius of ~1.05 Å, such that the middle REE has the maximum $D^{min/melt}$. Trivalent cations are generally compatible to highly compatible in Ca-perovskite giving it considerable leverage in crystallization models. Geochemical models based on these phase relations and partitioning results are used to test for evidence in mantle peridotite of preserved signals of crystal differentiation in a deep, Hadean magma ocean.

Model compositions for bulk silicate Earth and convecting mantle are constructed and evaluated. The model compositions for primitive convecting mantle yield superchondritic Mg/Si and Ca/Al ratios, although many refractory lithophile element ratios are near chondritic. Major element mass balance calculations effectively preclude a CI-chondritic bulk silicate Earth composition, and the super-chondritic Mg/Si ratio of the mantle is apparently a primary feature. Mass balance calculations indicate that 10–15% crystal fractionation of an assemblage dominated by Mg-perovskite, but with minor amounts of Ca-perovskite and ferropericlase, from a magma ocean with model peridotite-based bulk silicate Earth composition produces a residual magma that resembles closely the convecting mantle.

Partition coefficient based crystal fractionation models are developed that track changes in refractory lithophile major and trace element ratios in the residual magma (e.g. convecting mantle). Monomineralic crystallization of majorite or Mg-perovskite is limited to less than 5% before certain ratios fractionate beyond convecting mantle values. Only trace amounts of Ca-perovskite can be tolerated in isolation due to its remarkable ability to fractionate lithophile elements. Indeed, Ca-perovskite is limited to only a few percent in a deep mantle crystal assemblage. Removal from a magma ocean of approximately 13% of a deep mantle assemblage comprised of Mg-perovskite, Ca-perovskite and ferropericlase in the proportions 93:3:4 produces a residual magma with a superchondritic Ca/Al ratio matching that of the model convecting mantle. This amount of crystal separation generates fractionations in other refractory lithophile elements ratios that generally mimic those observed in the convecting mantle. Further, the residual magma is expected to have subchondritic Sm/Nd and Lu/Hf ratios. Modeling shows that up to 15% crystal separation of the deep mantle assemblage from an early magma ocean could have yielded a convecting mantle reservoir with $^{143}Nd/^{144}Nd$ and $^{176}Hf/^{177}Hf$ isotopic compositions that remain internal to the array observed for modern oceanic volcanic rocks. If kept in isolation, the residual magma and deep crystal piles would grow model isotopic compositions that are akin to enriched mantle 1 (EM1) and HIMU reservoirs, respectively, in Nd-Hf isotopic space.

1. INTRODUCTION

Most of Earth's mass accreted by numerous impacts between large bodies and proto-Earth (Chambers and Wetherill, 1998), and a giant impact with a Mars-sized object is the most plausible explanation for a Moon forming event (Canup and Asphaug, 2001). Physical models show that the energy buried in the proto-Earth from a giant impact would have raised interior temperatures by thousands of degrees, causing high degrees of melting and resulting in a global magma ocean (Benz and Cameron, 1990; Tonks and Melosh, 1993). Isentropic cooling of a magma ocean would lead to crystallization from the bottom up because liquidus crystallization curves have dT/dP slopes that are steep relative to a magma ocean adiabat. Numerical models indicate that vigorous convection during early stages of crystallization in a magma ocean may have effectively prevented accumulation of crystals (Tonks and Melosh, 1990; Solomatov, 2000). However, the possibility remains, perhaps especially during later stages of cooling, for considerable differentiation either by crystal fractionation or by melt expulsion due to compaction. If so, the primordial mantle may have had some nascent stratification (see for example Agee and Walker, 1988).

* Author to whom correspondence should be addressed (M.J.Walter@bristol.ac.uk).
† *Present address*: Department of Earth Sciences, University of Bristol, Wills Memorial Building, Queen's Road, BRISTOL, BS8 1RJ

Subsequent to initial layering, over 4 Ga of solid-state convection possibly re-homogenized most or all the mantle (e.g., van Keken et al., 2002). But a relic layer of early crystalline differentiates that formed in the deepest part of the magma ocean may have been resistant to homogenization due to intrinsic rheologic stability, possibly remaining buried in the deep lower mantle until the present. Such a deep layer may now reside in the region of the seismically imaged D "layer that extends as much as a few hundred kilometers above the core-mantle boundary" (e.g., Jeanloz and Williams, 1998), or could be a thicker layer potentially responsible for the apparent decrease in the correlation length in seismic heterogeneity observed at depths greater than ~1600 km (Kellogg et al., 1999; van der Hilst and Karason, 1999). An ancient buried layer is a potential storehouse for trace elements, including radioactive, heat-producing elements (e.g., Albarede and van der Hilst, 1999).

Segregation of mid to deep mantle liquidus phases such as majorite, Mg-perovskie (MgPv), Ca-perovskite (CaPv) and ferropericlase (FP) from an initially molten mantle may have led to fractionation between crystals and residual liquid of major and trace lithophile element ratios away from primitive mantle values (Agee and Walker, 1988; Kato et al., 1988; McFarlane et al., 1994; Presnall et al., 1998; Corgne and Wood, 2002). Crystal fractionation in the mantle, transient or permanent, could have had important effects on isotopic systems used to probe differentiation in the early mantle-crust system. Further, if the residual liquid crystallized into what is the modern convecting mantle, then a chemical signature of crystallization could be preserved in modern primitive upper mantle refractory lithophile element abundance ratios.

Here, we present new experimentally determined mineral/melt major and trace element partitioning data for liquidus phases of fertile mantle peridotite at deep mantle conditions. These data are used in combination with literature data for liquidus phase relations at lower mantle conditions (Trønnes and Frost, 2002; Ito et al., 2004), mineral/melt element partitioning for Ca-Pv (Corgne and Wood, 2002; Hirose et al., 2004), and model compositions for bulk silicate Earth and primitive upper mantle, for constructing geochemical models to probe for signals of early crystal differentiation in a deep magma ocean.

2. EXPERIMENTAL

We have determined phase relations and element partitioning among coexisting phases at the liquidus of a fertile model peridotite composition, PM-1, at pressures corresponding to the uppermost part of the lower mantle (~23–23.5 GPa). The major and trace element composition of PM-1 is given in Table 1. PM-1 was constructed by mixing Horomon plagioclase lherzolite with Komuro andesite in a ratio of 9:1 (Nakamura et al., 2001), proportions that yield near primitive mantle abundances of lithophile major and trace elements.

A finely powdered sample was dried in a vacuum oven at 120 °C to eliminate adsorbed water. Experiments were performed in a 'Kawai-type' multi-anvil apparatus using 10 mm edge length Cr-doped MgO octahedron and second-stage carbide anvils with truncations of either 4 or 3.75 mm. On the basis of room temperature and high temperature pressure calibration (e.g., Walter et al., 1995), the pressures in the experiments reported here are estimated at 23 to 23.5 ± 1 GPa. The sample was loaded into a cylindrical graphite capsule with an outer diameter of ~0.8 mm and an inner diameter of ~0.5 mm. The sample capsule is surrounded by MgO spacers, which in turn are surrounded by a cylindrical $LaCrO_3$ heater. All pressure cell parts, exclusive of the sample capsule, were fired at 1000 °C before assembly to eliminate moisture. The sample capsule was briefly heated in a gas flame to a 'red-hot' condition before loading the sample.

Table 1. Composition of primitive mantle starting composition, PM-1.

	PM-1[a]		PM-1	BSE[c]	CI[b]
	Wt.%			*ppm*	
SiO_2	45.74	Sr	51.38	21.1	7.25
TiO_2	0.21	Y	5.58	4.55	1.57
Al_2O_3	5.01	Zr	11.67	11.2	3.82
Cr_2O_3	0.27	Nb	0.26	0.71	0.24
FeO	8.07	Ba	16.42	6.99	2.41
MgO	34.57	La	0.82	0.69	0.24
CaO	3.86	Ce	2.12	1.78	0.61
MnO	0.14	Pr	0.33	0.28	0.09
NiO	0.20	Nd	1.64	1.35	0.46
Na_2O	0.59	Sm	0.55	0.44	0.15
K_2O	0.08	Eu	0.2	0.17	0.06
Total	98.74	Gd	0.71	0.6	0.2
		Dy	0.87	0.74	0.25
Mg#	88.3	Er	0.53	0.48	0.16
MgO/SiO_2	0.76	Yb	0.58	0.49	0.16
CaO/Al_2O_3	0.77	Lu	0.09	0.07	0.02
CaO/TiO_2	18	Hf	0.36	0.31	0.1

[a] Starting composition for experiments.
[b] Cl-chondrite of McDonough and Sun (1995).
[c] Bulk silicate Earth of McDonough and Sun (1995).

The objective of these experiments was to produce melt coexisting with well-equilibrated crystals large enough for accurate trace element analysis using secondary ion mass spectrometry (SIMS). To achieve this goal requires stable, long duration experiments. It is our experience that at the required high temperatures (e.g., ~2300 °C), W/Re thermocouples are frequently unreliable in long experiments (see also Lesher et al., 2003). Further, insertion of a thermocouple and surrounding insulator produces an asymmetric temperature distribution in the cell, and these parts can also have an adverse effect on the stability of the $LaCrO_3$ heater (Walter et al., 1995). We have chosen to eliminate the thermocouple entirely from our assembly, and instead of controlling temperature at constant thermocouple *emf*, experiments were held at a constant power setting. We first made several runs with W/Re thermocouples to establish a power versus temperature working curve, and then eliminated the thermocouple once a working power range was determined. After ramping to the set power, constant power was maintained for 50 to 60 min with a precision of ~0.2% relative. After an initial settling-in time of ~5 min, heater electrical characteristics (voltage, current, power, resistance) all remained constant throughout the run duration. We presume temperature remained essentially constant as well.

A composite backscattered-electron image of the melted portion of the charge in experiment #249 is shown for reference in Figure 1. The quenched-melt phase is generally expelled

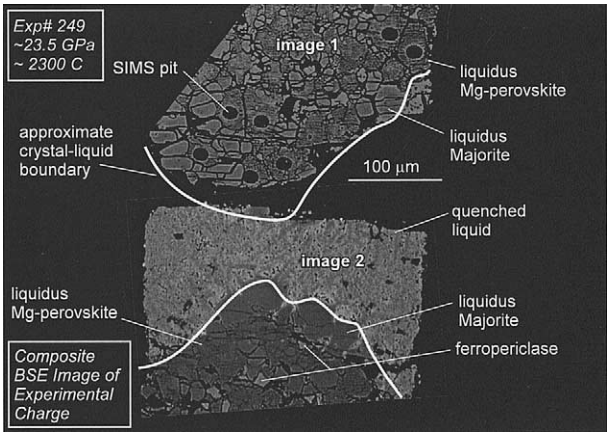

Fig. 1. A composite backscattered-electron image of the melted portion in experiment #249, taken at a magnification of 370X. The charge broke into two pieces along a boundary between quenched melt and crystals, and two separate images are combined to form an approximate reconstruction of the charge. Ion erosion pits from the SIMS analysis are readily apparent in image 1.

from the crystalline portion of the charge, with the exception of a 'mushy' crystal-liquid interface. Melt expulsion due to thermally induced crystal compaction will always occur in a temperature gradient (Lesher and Walker, 1988). To facilitate equilibrium between partial melt and crystals, it is prudent to keep temperature gradients to a minimum in partitioning experiments (Walker and Agee, 1989).

The graphite sample capsule transforms to polycrystalline diamond during the experiment, and due to the extremely high thermal conductivity of diamond and the small size of the capsule, the sample temperature gradient across the sample is much less than in a metal capsule. This was exemplified by (1) polymineralic and only moderately curved liquidus boundaries, as opposed to monomineralic and highly curved boundaries commonly observed at the liquidus in long experiments made in a large temperature gradient (e.g., Presnall and Walter, 1993), (2) large (~40–50 μm) liquidus phases 'floating' in the quenched-melt and melt embayment into the crystalline region, and (3) constant quenched-melt composition across the melted region. The diamond capsule is not readily polished. However, we found that during quench, pervasive horizontal fractures develop along the axis of the diamond portion of the capsule. By digging around the capsule with a micro-drill, the diamond capsule is easily fragmented and removed with a pair of fine tweezers, allowing retrieval of the sample cylinder.

Here we present results from two experiments that are summarized in Table 2. Run# 62 was made at a nominal pressure of 23 GPa and was held at 620 ± 1 W for 50 min. Run# 249 (Fig. 1) was made at a nominal pressure of 23.5 GPa and held at 620 ± 1 W for 60 min. The temperature in both runs is estimated at 2300 ± 100 °C based on runs calibrated with W/Re thermocouples.

3. PHASE RELATIONS

Phase identification was made using SEM and BSE imaging. In run #62 the central portion of the charge contained a large region of melt, ~200 × 300 μm. Crystalline phases are present in a symmetrical distribution about the melt region. Large crystals of majorite (~50 μm diameter) and a few smaller FP grains are scattered along the interface in direct contact with the melt. About 20 to 30 μm back from the melt-solid interface, large (20–40 μm diameter) crystals of MgPv with clearly discernable euhedral grain shape and typical polysynthetic twin lamellae are intergrown with majorite and FP. Based on a mass balance calculation using major element compositions of coexisting phases (Table 2), the sample was ~60% molten.

In run #249 the melted region was smaller, ~100 × 200 μm (Fig. 1), and mass balance indicates ~45% melting. The solid-melt interface is not as sharply defined as in run #62, as large euhedral crystals of majorite (~50 μm diameter) are 'floating' in the melt, with melt embayment into the polymineralic crystalline portion. In contrast to run #62, large crystals of MgPv (~20 to 40 μm diameter) are in direct contact with the melt. FP is present within ~20 μm of the solid-melt boundary.

We interpret the phase relations in these runs within the context of the phase relations between 23 and 25 GPa for fertile peridotite presented by Trønnes and Frost (2002). In their phase diagram, majorite, MgPv, and FP crystallize together upon cooling below the liquidus within the pressure range of ~23 to 24.5 GPa. FP is the liquidus phase for nearly all of that pressure range, followed down-temperature by majorite up to ~23.8 GPa, and then MgPv at higher pressure. The maximum pressure of majorite stability in the liquidus interval is ~24.5 GPa. At ~23 GPa majorite becomes the liquidus phase followed closely down-temperature by FP, and only near the solidus does MgPv appear.

Run #62 apparently crystallized majorite and FP together at the liquidus, although it is difficult to discern which is the liquidus phase, followed closely down-temperature by MgPv. In run #249 majorite and MgPv are in direct contact with melt (Fig. 1). Majorite is probably the liquidus phase as it alone is floating away from a polymineralic melt-solid interface. Run #249 was at a slightly higher pressure (smaller anvil truncation at same press load), perhaps ~0.5 GPa, than run #62. If

Table 2. Experimental conditions and liquidus phases.

Run#	Load[a]	P (GPa)[b]	Watts	T (°C)[c]	Time (min)	Phases[d]
62	1018	~23	620	~2300	50	62 melt: 26 MgPv: 9 Maj: 3 FP
249	1018	~23.5	620	~2300	60	46 melt: 26 MgPv: 23 Maj: 5 FP

[a] Press load in metric tons using 5000 ton press at ISEI.
[b] Run# 62 made with 4 mm anvil truncations, and run# 249 with 3.75 mm truncations.
[c] Estimated from power-temperature calibration and phase relations of Trønnes and Frost (2002).
[d] Phase proportions calculated by mass balance.

Table 3. Major and minor element compositions of coexisting phases (weight%).

	Melt	MgPv	Majorite	FP	Melt	MgPv	Majorite
Exp #62					Exp #249		
	14	10	5	3	12	20	12
SiO_2	46.49 (90)[a]	54.70 (67)	52.28 (42)	0.18 (5)	44.75 (76)	55.08 (25)	52.09 (30)
TiO_2	0.24 (2)	0.26 (6)	0.01 (1)	0.001 (1)	0.27 (2)	0.25 (4)	0.02 (1)
Al_2O_3	3.22 (13)	4.27 (46)	11.02 (25)	1.16 (32)	2.42 (12)	3.21 (13)	9.97 (25)
Cr_2O_3	0.23 (1)	0.24 (3)	0.30 (2)	0.37 (2)	0.24 (1)	0.23 (2)	0.33 (1)
FeO	6.23 (29)	4.23 (61)	1.98 (4)	9.90 (6)	9.15 (40)	4.44 (27)	2.92 (4)
MgO	34.46 (65)	35.48 (51)	30.98 (36)	86.04 (46)	32.04 (66)	35.65 (39)	30.76 (17)
CaO	7.13 (20)	0.79 (14)	3.64 (17)	0.06 (22)	8.36 (24)	0.84 (13)	4.32 (13)
MnO	0.14 (1)	0.07 (2)	0.07 (1)	0.12 (1)	0.19 (1)	0.09 (1)	0.1 (1)
NiO	0.11 (1)	0.05 (2)	0.05 (3)	0.52 (3)	0.16 (1)	0.06 (1)	0.05 (1)
Na_2O	0.43 (4)	0.05 (1)	0.15 (2)	0.27 (2)	0.60 (4)	0.06 (1)	0.29 (1)
K_2O	0.05 (1)	0.01 (1)	0.01 (1)	0.002 (1)	0.09 (1)	0.01 (1)	0.01 (1)
Total	98.73 (27)	100.15 (67)	100.49	98.62	98.27 (58)	99.92	100.86
Cations per:		3 oxygen	12 oxygen	1 oxygen		3 oxygen	12 oxygen
Si^{4+}		0.94	3.56	0.001		0.95	3.56
Ti^{4+}		0.004	0.001	—		0.004	0.001
Al^{3+}		0.086	0.88	0.010		0.065	0.80
Cr^{3+}		0.003	0.016	0.002		0.003	0.018
Fe^{2+}		0.061	0.113	0.059		0.064	0.17
Mg^{2+}		0.906	3.14	0.91		0.91	3.13
Ca^{2+}		0.015	0.27	0.0005		0.016	0.32
Mn^{2+}		0.001	0.004	0.0007		0.001	0.006
Ni^{2+}		0.001	0.003	0.003		0.001	0.003
Na^{1+}		0.002	0.02	0.004		0.002	0.04
K^{1+}		0.0001	0.0004	—		0.0001	0.001
Total		2.01	8.01	0.99		2.02	8.05

[a] Uncertainty is one standard error of the mean in least significant digits.

majorite is the liquidus phase in #249, then phase relations dictate that it must be in lower pressure run #62 as well. The increase in pressure also seems to have expanded the MgPv field as it coexists on the liquidus with majorite. Starting composition PM-1 is very similar to but somewhat more alumina- and silica-rich than the compositions used by Trønnes and Frost (2002) ('Pyrolite' and KLB-1), and the association of the phases in our experiments to the liquidus indicate expansion of the majorite crystallization field to somewhat higher pressures, and also expansion of the MgPv field relative to FP.

4. ANALYTICAL

Major and minor element compositions of coexisting phases were determined using a JEOL8800 EPMA (Table 3). A beam current of 30 nA and an acceleration voltage of 15 kV were used in all analyses. Spot size was 5–10 μm in diameter for mineral phases and 10 to 20 μm in diameter for quenched melt. Na and K were analyzed first to reduce effects of volatilization and migration during analysis. Calibration was made using a set of oxide and silicate standards, and raw counts were converted to oxide weight% using a Phi-Rho-Z algorithm. Counting times were 30 to 40 s on peak and 10 to 20 s on background. Analytical precision is better than 2% relative for major elements and 5% relative for minor elements. There were no systematic variations within major element uncertainty across the melt region (probe points a minimum of 30 μm away from a primary crystal interface), indicating that temperature gradients were low enough for Soret effects to be undetectable.

Trace element analyses of minerals and quenched melt were made with a Cameca ims 5f ion microprobe following techniques similar to those described in (Nakamura and Kushiro, 1998), and the results are given in Table 4. Due to the long run durations at extreme temperature, the samples are contaminated by La derived from the $LaCrO_3$ furnace. The quenched melts in runs #62 and #249 contain ~2600 and 1000 ppm La, respectively. High La contents cause extreme isobaric mass interference especially in the middle REE, making it difficult to apply the energy offset method together with subtraction of the interferences empirically determined for common minerals and glasses (Nakamura and Kushiro, 1998). To minimize the strong interferences in the REE analyses, we applied a matrix-matching technique by synthesizing MORB glasses with La concentrations ranging from 50 to 3000 ppm. Six homogeneous glasses were synthesized in a piston cylinder apparatus at 1 GPa and 1400 °C for 1 h. Trace element abundances in the synthesized glasses were precisely characterized using ICP-MS (Makishima and Nakamura, 1997).

The following procedure was adopted for measuring trace element abundances in the melt phase of the experimental charges. First we measured the apparent La concentration using LREE-enriched alkaline basalt glass as a standard. Once the La concentration in the melt was determined, a synthesized glass standard with a similar La concentration was used for calibration of all trace element abundances. Mineral phases are relatively enriched in middle to heavy REE resulting in much less influence of La contamination compared with the case for quench, so we applied our common standardization method using clinopyroxene and garnet from mantle xenoliths as standard materials. Trace elemental compositions of these standard minerals have been determined precisely by ICP-MS (Ma-

Table 4. Trace element compositions of coexisting phases (ppm).

	Melt	MgPv	Majorite	FP
Exp #62				
n	12	8	8	2
Li	2.58 (7)[a]	0.212 (82)	0.185 (11)	—
Sr	81.4 (14)	1.282 (37)	1.52 (4)	1.67 (6)
Y	35.8 (4)	8.64 (128)	10.2 (2)	1.06 (6)
Zr	176 (2)	273 (53)	25.0 (26)	32.1 (202)
Nb	1.86 (3)	0.022 (3)	0.003 (1)	0.005 (2)
Ba	28.8 (10)	1.12 (29)	0.34 (7)	21.5 (36)
La	2252 (21)	4.25 (77)	8.49 (53)	30.21 (30)
Ce	11.4 (4)	0.18 (2)	0.095 (7)	0.26 (22)
Pr	1.43 (3)	0.027 (4)	0.026 (3)	0.093 (8)
Nd	6.65 (19)	0.25 (3)	0.21 (1)	0.30 (30)
Sm	1.89 (8)	0.13 (2)	0.13 (2)	0.11 (10)
Eu	0.63 (5)	0.046 (7)	0.052 (4)	0.021 (13)
Gd	2.97 (20)	0.32 (5)	0.26 (2)	0.41 (7)
Dy	4.13 (35)	0.66 (8)	0.72 (3)	0.13 (11)
Er	1.78 (27)	0.74 (10)	0.58 (3)	0.31 (21)
Yb	1.46 (11)	0.84 (7)	0.70 (5)	0.12 (2)
Lu	0.14 (2)	0.12 (2)	0.11 (1)	0.027 (15)
Hf	1.35 (18)	2.21 (42)	0.32 (4)	0.322 (11)
Exp #249				
n	11	8	3	
Sr	180 (10)	4.09 (80)	3.86 (142)	
Y	18.2 (2)	4.47 (63)	5.92 (29)	
Zr	117 (2)	159 (41)	14.5 (13)	
Nb	2.11 (9)	0.024 (3)	0.003 (1)	
Ba	213 (2)	8.60 (142)	3.70 (54)	
La	998 (5)	5.00 (110)	6.97 (405)	
Ce	7.54 (32)	0.25 (3)	0.13 (7)	
Pr	1.31 (5)	0.032 (6)	0.025 (5)	
Nd	5.71 (20)	0.18 (3)	0.13 (3)	
Sm	1.51 (10)	0.092 (19)	0.072 (20)	
Eu	0.49 (5)	0.036 (8)	0.023 (6)	
Gd	3.60 (34)	0.56 (15)	0.79 (23)	
Dy	2.93 (9)	0.48 (7)	0.48 (3)	
Er	1.71 (8)	0.49 (7)	0.61 (1)	
Yb	0.88 (4)	0.67 (7)	0.45 (5)	
Lu	0.11 (1)	0.11 (1)	0.093 (9)	
Hf	1.91 (6)	2.44 (52)	0.30 (4)	

[a] Error is one standard error of the mean in least significant digits.

kishima and Nakamura, 1997). The results obtained using either clinopyroxene or garnet were identical within analytical uncertainty.

Minerals were sputtered with O- primary beams of 5 to 7 nA intensity resulting in a beam diameter of 10–15 μm on the mineral surface. The quenched melt portion was probed using a primary beam current of 10 nA, and the beam was rastered across a 50 $\times$ 50 μm area. Positive secondary ions were collected by ion counting using an energy offset of -60 V and -90 V for mineral and glass, respectively, from 4500 V acceleration with an energy bandpass of ± 10 V. Analytical reproducibility determined for one of the clinopyroxene standards was generally better than 10%, except for Ba (50%), but typically better than 5% for La, Sm and Gd.

5. ELEMENT PARTITIONING

The Nernst partition coefficient, D, describing the distribution of an element between mineral and melt, is defined as:

$$D_i^{min/melt} = X_i \text{ in the mineral}/X_i \text{ in the melt} \quad (1)$$

where X_i is the weight fraction of element i. Major, minor and trace element partition coefficients are given in Table 5.

Elemental partitioning is in part dictated by crystal chemistry, so a brief review is appropriate (see also Finger and Hazen, 2000). Ca-bearing majorite ($^{VIII}A_3{}^{VI}B_2{}^{IV}Si_3O_{12}$) crystallizes in a tetragonal structure (space group $I4_1/a$) with seven crystallographically distinct cation sites (e.g., Hazen et al., 1994). Mg^{2+}, Ca^{2+} and Fe^{2+} are principle cations in two large dodecahedral (eightfold) sites (A). Two octahedral (six-fold) sites (B) are occupied by Al^{3+} and Fe^{3+} as well as Mg^{2+} and Si^{4+} involved in coupled substitution. Three tetrahedral (fourfold) sites are occupied principally by Si^{4+}. Large monovalent, divalent and trivalent trace cations are probably incorporated principally in the large eightfold sites, whereas smaller highly charged cations may mix into the octahedral or tetrahedral sites.

MgPv (ABO_3) crystallizes in an orthorhombic structure (space group *Pbmn*) with a large, distorted eightfold site (A) and a smaller octahedral site (B) (e.g., Horiuchi et al., 1987). Divalent major element cations (e.g., Ca, Mg, Fe^{2+}) reside in the eightfold site, whereas Si^{4+} resides in the octahedral site. Although there is still debate about the substitution mechanisms, Al^{3+} may mix into A and B sites via coupled substitution with Mg^{2+} and Si^{4+}, or into the B site accompanied by vacancy formation (e.g., Andrault et al., 1998; Richmond and Brodholt, 1998). A coupled substitution of Al^{3+} and Fe^{3+} for Si^{4+} and Mg^{2+} is also likely, with Fe^{3+} mixing into the A site and Al^{3+} into the B site (e.g., Frost and Langenhorst, 2002). Monovalent, divalent and trivalent trace cations probably enter exclusively into the large eightfold site, whereas smaller highly charged cations may mix into the octahedral site (e.g., Andrault, 2003).

FP (AO) crystallizes in the cubic rock-salt structure (space group *Fm3m*) with an octahedral site (A) occupied nominally by divalent cations Mg and Fe. Heterovalent substitution of minor and trace cations also occurs on this site.

Figure 2 shows major element partitioning of cations between minerals and melt in runs #62 and #249. For comparative purposes, partitioning results from an experiment at 24 GPa using KLB-1 as starting material from the recent work of Trønnes and Frost (2002) are also shown. Si, Ti, Al, Cr and Mg are all compatible in MgPv, whereas other major and minor elements are incompatible. Ca is markedly incompatible in MgPv. Overall there is good agreement between our results and those of Trønnes and Frost (2002), although we find Ca to be markedly less compatible.

Si, Cr, and Mg all have Ds near unity in majorite, whereas Al is very compatible with a $D > 3$. Other elements are incompatible. Relative to MgPv, Ca is considerably more compatible in majorite, mixing more easily into a larger eightfold site. Conversely, Ti is much less compatible in majorite than in MgPv. In MgPv Ti mixes easily into the octahedral B site that is normally occupied by Si^{4+}, but due to its relatively large cation radius is readily excluded from the tetrahedral site in majorite. It is worth noting that Trønnes and Frost (2002) found Ti, and to a lesser extent Ca, to be considerably more compatible in majorite than in the present study.

Mg, Fe, Cr and Ni are compatible in FP, whereas other elements are incompatible. Si, Ti and Ca are all strongly excluded from the FP structure. There is generally good agreement with the results of Trønnes and Frost (2002), again with

Table 5. Mineral/Melt partition coefficients.

	#62 MgPv	#249 MgPv	#62 Maj	#249 Maj	#62 FP
Si	1.21 (2)[a]	1.28 (2)	1.16 (1)	1.20 (2)	0.003 (5)
Ti	1.11 (17)	0.96 (11)	0.05 (3)	0.08 (2)	0.004 (3)
Al	1.36 (11)	1.38 (7)	3.52 (13)	4.24 (17)	0.32 (6)
Cr	1.03 (10)	1.00 (7)	1.32 (7)	1.42 (7)	1.42 (9)
Fe	0.70 (7)	0.51 (3)	0.33 (1)	0.33 (1)	1.43 (4)
Mg	1.06 (2)	1.16 (2)	0.92 (2)	0.99 (2)	2.24 (3)
Ca	0.11 (1)	0.10 (1)	0.52 (3)	0.53 (2)	0.01 (1)
Mn	0.52 (10)	0.49 (4)	0.51 (6)	0.54 (4)	0.78 (8)
Ni	0.47 (12)	0.39 (5)	0.45 (17)	0.32 (5)	4.40 (43)
Na	0.11 (2)	0.10 (2)	0.36 (5)	0.50 (3)	0.56 (6)
K	0.21 (10)	0.12 (4)	0.10 (13)	0.11 (4)	0.072 (34)
Li	0.082 (33)	—	0.072 (6)	—	—
Sr	0.016 (5)	0.023 (6)	0.019 (7)	0.021 (9)	0.017 (1)
Y	0.24 (4)	0.25 (4)	0.28 (10)	0.33 (2)	0.027 (2)
Zr	1.55 (32)	1.36 (39)	0.14 (5)	0.12 (2)	0.15 (15)
Nb	0.012 (2)	0.011 (2)	0.002 (1)	0.0012 (2)	0.002 (1)
Ba	0.039 (12)	0.040 (1)	0.012 (5)	0.017 (4)	0.64 (22)
La	0.002 (1)	0.005 (1)	0.004 (1)	0.007 (5)	0.011 (16)
Ce	0.016 (3)	0.033 (7)	0.008 (3)	0.017 (10)	0.016 (2)
Pr	0.019 (3)	0.024 (6)	0.018 (7)	0.019 (5)	0.051 (6)
Nd	0.038 (5)	0.032 (8)	0.031 (12)	0.022 (6)	0.036 (52)
Sm	0.067 (13)	0.061 (18)	0.069 (28)	0.048 (16)	0.049 (62)
Eu	0.072 (18)	0.074 (2)	0.082 (36)	0.048 (18)	0.023 (20)
Gd	0.11 (3)	0.15 (6)	0.088 (37)	0.22 (9)	0.067 (17)
Dy	0.16 (3)	0.16 (3)	0.17 (7)	0.16 (2)	0.017 (19)
Er	0.42 (12)	0.28 (6)	0.32 (17)	0.36 (3)	0.040 (40)
Yb	0.58 (10)	0.77 (13)	0.48 (21)	0.52 (8)	0.050 (9)
Lu	0.91 (28)	0.99 (21)	0.78 (40)	0.83 (16)	0.11 (9)
Hf	1.64 (54)	1.28 (32)	0.23 (12)	0.16 (3)	0.076 (40)

[a] Uncertainty based on standard error of melt and mineral phases.

the exception of Ti and Ca, which were found more compatible in that study.

Figure 3 shows trace element partition coefficients for cations between minerals and melt in runs #62 and #249. There is excellent agreement between the two experiments. In general, trace elements are incompatible in MgPv, with the exception of the HFSE, Hf and Zr, which have Ds slightly greater than unity. In contrast, Nb is markedly incompatible. LREE are very incompatible, but compatibility increases monotonically from LREE to HREE. Trace element partitioning into majorite is remarkably similar to MgPv, with the notable exception of Hf and Zr, which are incompatible in majorite. As a group the REE Ds are nearly identical in the two minerals. Overall, trace elements are very incompatible in ferropericlase.

Ba, with its large ionic radius (~1.42 Å) in eightfold coordination (Shannon, 1976), is typically a highly incompatible element. We note that D^{Ba} seems unusually high in FP, MgPv and majorite, as it is larger than D^{La} in all three phases. Ba is potentially a marker for SIMS beam overlap onto the melt phase, or of melt inclusions, during analysis of the solid. There are several observations that argue against such melt contamination. First, we note that Nb and La, which are also highly incompatible, do not show unusually large D values. The melt phase is similarly enriched relative to the solid in these elements, and should show similar anomalies to Ba. In fact, because the melts produced in this study are unusually enriched in La, D^{La} should be most sensitive to melt contamination, but as we show below, D^{La} measured here is actually lower for both majorite and MgPv than in other recent studies. One discarded FP analysis clearly overlapped the glass, and all incompatible element Ds increased proportionally. Second, MgPv and majorite grains were large relative to the ion beam, with analyzed grains typically 30 to 50 μm in diameter (ion beam diameter ~10 to 20 μm, see Fig. 1). We note that standard reproducibility is poorer for Ba, but standard errors for Ba abundance remain generally similar to other elements, whereas random inclusion of a melt component should yield larger standard errors for Ba.

5.1. Lattice Strain Model of Element Partitioning

Element partitioning into minerals may be modeled according to ionic, lattice-strain theory (see for example Blundy and Wood, 2003). The incorporation of a trace cation, *i*, into a crystallographic site with an ideal radius, r_o, and an ideal cation charge, Z_o, will depend primarily on the size and charge of the substituting cation. A size mismatch will cause an energy penalty related to the lattice strain energy in 'fitting' cation *i* into the site, which is related to the Young's modulus (*E*) of the site. For a given cation charge, the partition coefficient of a cation with the ideal site radius is a maximum, D_o, and values of *D* for mismatched cations have a near-parabolic dependence on cation size (Blundy and Wood, 1994). An energy penalty is also paid for the amount of charge mismatch relative to the charge of the host cation, and *D* may also have a parabolic dependence on the amount of charge mismatch (Wood and Blundy, 2001). The lattice strain model has proven effective as a predictive tool for trace element partitioning in a number of

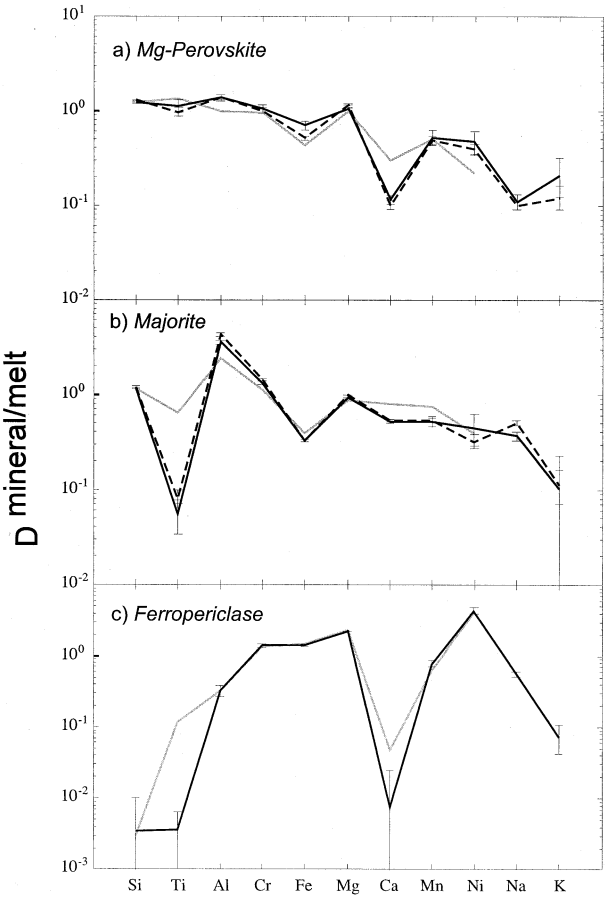

Fig. 2. Major element mineral/melt partition coefficients from Table 5. Solid black line is for experiment #62. Dashed line is for experiment #249. Shaded line is data from Trønnes and Frost (2002). Error bars are ±2 standard error of the mean.

mantle silicates (e.g., Blundy and Wood, 1994; Wood and Blundy, 1997; van Westrenen et al., 1999), but it should be noted that melt composition may also play an important role in partitioning, and its effects are just beginning to be systematically explored.

Here, we have used our new data to develop lattice-strain models for partitioning of divalent and trivalent cations in majorite and MgPv, and have used recent literature data to model partitioning of trivalent cations in CaPv. Partitioning data are regressed to the lattice-strain equation of Blundy and Wood (1994), where:

$$D_i = D_o \exp\left(\frac{-4\pi E_s N_A\left(\frac{r_o}{2}(r_i - r_o)^2 + \frac{1}{3}(r_i - r_o)^3\right)}{RT}\right) \quad (2)$$

where D_i is the partition coefficient of element i, E_s is the Young's Modulus of the site, N_A is Avogadro's number, r_o is the ideal crystallographic site radius, D_o is the partition coefficient of an element with the ideal site radius, r_i is the ionic radius of element i in the site of interest, R is the gas constant and T is temperature in K.

5.1.1. *Majorite and Mg-perovskite*

Results of regressions to the lattice strain equation for divalent and trivalent cations in eightfold coordination are given in Table 6, and are illustrated in Figures 4 and 5. We have taken the approach of using only Mg, Ca and Sr to define an eightfold site parabola, excluding transition elements like Fe, Mn and Ni that are susceptible to crystal field effects (Wood and Blundy, 1997). Figure 4 shows that partitioning data for majorite and MgPv from this study and from Corgne and Wood (2004) and Corgne et al. (2003) generate a very compatible set of lattice strain models. The ideal site radius for divalent cations is about 1.0 Å for majorite and close to 0.9 Å for MgPv, and consequently Ca is more compatible in majorite.

Measured values of D^{Ba} are orders of magnitude larger than predicted by the lattice strain model in both minerals. We noted above that D^{Ba} is unusually large in our experiments relative to, for example, La. Corgne and Wood (2004) measure a comparably high D^{Ba} for majorite, helping to establish the position we were compelled to take above that the values are legitimate. We note that D^{Sr} for MgPv is also large relative to the model. One potential explanation for a large D^{Ba} is that Ba^{2+}, which has an ionic radius very near that of O^{2-}, substitutes for oxygen in a reaction that forms a Si^{4+} vacancy (e.g., $Ba^{2+} \leftrightarrow O^{2-} + Si^{4+}$: B. Wood, personal communication).

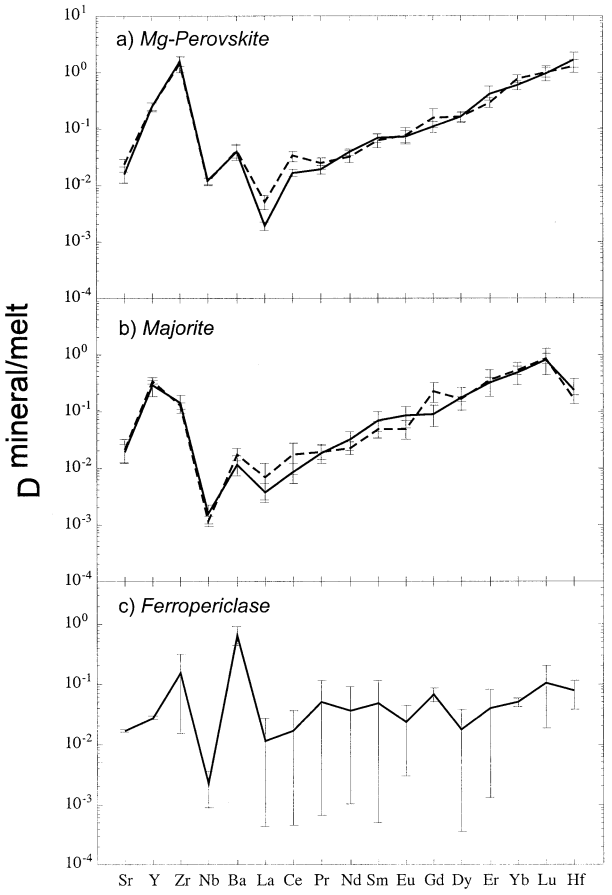

Fig. 3. Trace element mineral/melt partition coefficients from Table 5. Solid black line is for experiment #62. Dashed line is for experiment #249. Error bars are ±2 standard error of the mean.

Table 6. Regression parameters to the lattice-strain equation for 8-fold divalent and trivalent cations in Mg-perovskite.

	E (GPa)	r_o (Å)	D_o	Comment
Majorite				
2+	275 (38)	0.99 (1)[a]	1.38 (12)	this study (Mg, Ca, Sr)[d]
2+	282 (14)	1.0 (1)[a]	1.45 (8)	Corgne and Wood (2004)[e]
3+	432 (37)	0.91[b]	0.60 (10)	this study
3+	352 (29)	0.88[c]	0.85 (15)	this study
3+	377 (26)	0.88 (1)[a]	1.21 (10)	Corgne and Wood (2004)
Mg-Perovskite				
2+	236 (16)	0.89[b]	1.11 (2)	this study (Mg, Ca, Sr)[d]
2+	217 (73)	0.93 (3)[a]	1.24 (3)	Corgne et al. (2004)[f]
2+	303 (20)	0.94 (1)[a]	1.72 (14)	Hirose et al. (2004)
3+	378 (34)	0.89[b]	0.79 (17)	this study
3+	301 (27)	0.84[c]	1.39 (35)	this study
3+	752 (72)	0.89[b]	2.03 (21)	this study, D^{Sc} fixed at 2.0
3+	341 (47)	0.84 (2)[a]	2.67 (14)	Corgne et al. (2004)
3+	143 (17)	0.84[c]	0.77 (14)	Hirose et al. (2004)

[a] Free parameter in regression.
[b] Value is fixed in the regression, estimated on the basis of the weighted ionic radius of Ca, Mg, and total Fe in 8-fold sites. We assume $Fe^{3+}/[Fe^{2+} + Fe^{3+}] = 0.5$.
[c] Estimated value, fixed in regression.
[d] D^{Mg} in these calculations for majorite is based on a structural formula in which Mg is allocated between 8- and 6-fold sites, as required by coupled substitution involving trivalent cations (e.g. Al^{3+}, Fe^{3+}, Cr^{3+}).
[e] Regressed to data reported in Corgne and Wood (2004).
[f] Regressions to 'preliminary' data of Corgne et al. (2003).

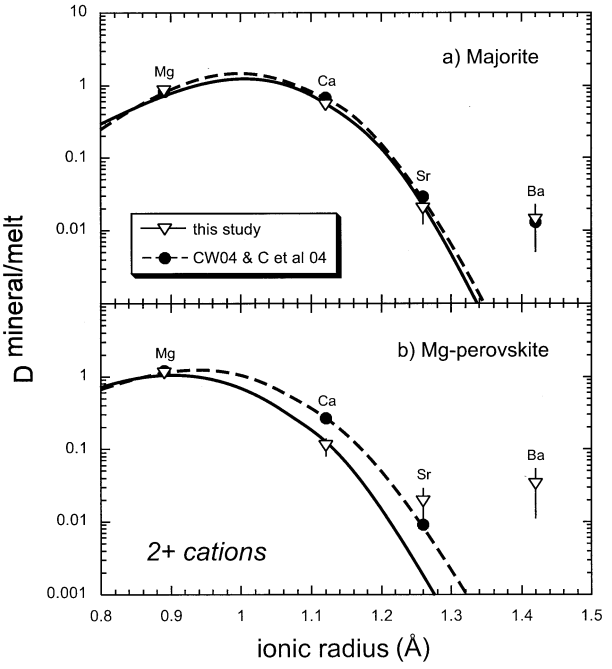

Fig. 4. Partition coefficients for divalent cations in eightfold coordination as a function of ionic radius (Å) for (a) majorite and (b) MgPv. Inverted diamonds are data from this study, and Ds are averages of experiments #62 and #249. Circles are data from Corgne and Wood (2004) for majorite and Corgne et al. (2003)for MgPv. Ionic radii are from (Shannon; 1976). D^{Mg} for majorite is based on a structural formula in which Mg^{2+} is allocated between 8- and sixfold sites, as required by coupled substitution involving trivalent cations (e.g., Al^{3+}, Fe^{3+}, Cr^{3+}). Parabolas show lattice-strain models based on parameters given in Table 6.

Lattice strain models for trivalent cations in eightfold sites are shown in Figure 5. Partitioning data from Corgne et al. (2003), Corgne and Wood (2004) and Hirose et al. (2004) are also shown. A difficulty arises in modeling these data because nearly all the elemental ionic radii fall to one side of a lattice strain parabola. Sc alleviates this problem, but has been measured only in the experiments of Corgne et al. (2003) and Corgne and Wood (2004). In modeling our data, we began by estimating the ideal site radii, r_o, in majorite and MgPv on the basis of weighting the ionic radii of divalent major element cations in eightfold coordination, yielding values of 0.91 Å and 0.89 Å for these minerals, respectively. These values were then fixed in regressions (Table 6). A regression to the majorite data of Corgne and Wood (2004) with r_o as a free parameter yields a value of 0.88 Å, and we also regressed our majorite data using this value. A regression to the MgPv data of Corgne et al. (2003) with r_o as a free parameter yields a value of 0.84 Å, and again, we regressed our data assuming that value as well.

Overall there is generally good agreement between the data of Corgne and coworkers and our data for both majorite and MgPv, with the primary difference being that D_0 is generally somewhat lower for our data. This has important implications for predicted values of D^{Sc}, which is either 0.8 or 1.4 in regressions to our MgPv data depending on the fixed value of r_o, either 0.89 Å or 0.84 Å (Table 6). It turns out that Sc is an important element in the geochemical modeling presented below. Previous measurements of D^{Sc} for MgPv indicate that it is compatible. For example, Drake et al. (1993) measured a value of 1.6, Corgne et al. (2003) a value of ~2, and Kato et al. (1988) reported a value close to 3, which was revised downward from an even higher value near 5. There is likely to be a dependence of r_o on mineral composition. Because the ionic radius of Sc^{3+} corresponds closely to the ideal site radius and the strain parabola are fairly tight, D^{Sc} will also have compo-

sitional dependence, and the relative compatibility of Sc to the HREE could change considerably, or even invert. Until a direct measurement of Sc is made in our experiments, we prefer to use the model regressed to our data for MgPv with an r_0 of 0.84 Å, which yields Sc compatible in MgPv ($D^{Sc} = 1.4$). We note, however, that if we fix D^{Sc} to 2 in a regression to our data, an unusually large Young's modulus is required (Table 6).

It is apparent on Figure 5 that deviations among studies become progressively larger with increase in ionic radius. The recent data of Hirose et al. (2004) for MgPv indicate a distinct change in slope near the ionic radius of Dy, prompting these authors to suggest the possibility of two distinct crystallographic sites in MgPv. Regressions for each site independently yielded Young's modulii of over 1500 GPa. An alternative explanation is that cation diffusivities of REE in MgPv increase with ionic radii. We note that, Ce notwithstanding, partition coefficients measured in this study for the mid to light-REE tend to be the lowest measured among recent studies, whereas those measured by (Hirose et al., 2004) are the highest and data from Corgne et al. (2004) intermediate. This sequence correlates directly with experiment duration, with Hirose et al.'s experiments the shortest (~2 min) and those here the longest (~60 min). Support for time-dependent partitioning comes from the majorite-melt partitioning study of Nakamura et al. (2001). These authors reported that partition coefficients of highly incompatible elements (e.g., La, Nb) became progressively lower with experiment duration, and that a time of the order 60 min was required to achieve a steady state at 2400 °C.

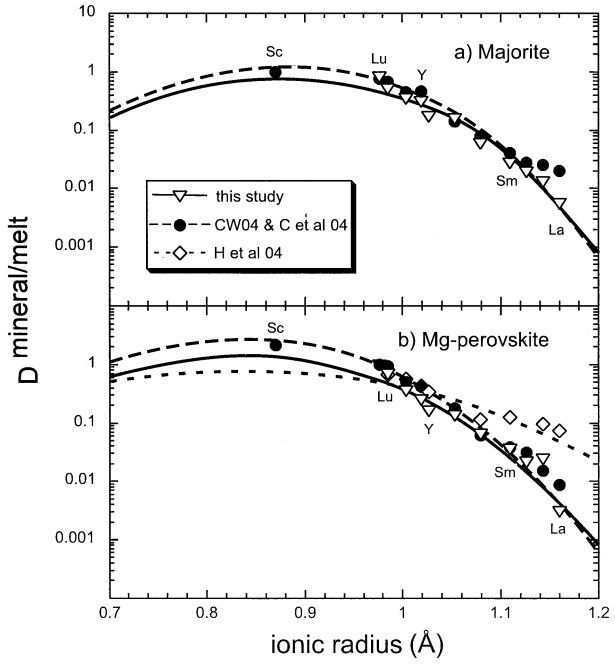

Fig. 5. Partition coefficients for trivalent cations in eightfold coordination as a function of ionic radius (Å) for (a) majorite and (b) MgPv. Inverted diamonds are data from this study, and Ds are averages of experiments #62 and #249. Circles are data from Corgne and Wood (2004) for majorite and Corgne et al. (2003) for MgPv. Diamonds are data from Hirose et al. (2004) for MgPv. Ionic radii are from (Shannon, 1976). Parabolas show lattice-strain models based on parameters given in Table 6.

Table 7. Regression parameters to the lattice-strain equation for trivalent cations in Ca-perovskite, and parameterizations for D^{Ca}, D^{Al}, and D^{Zr}.

	E (GPa)	r_o (Å)	D_o	Resnorm	Comment
3+[a]	312	1.05[b]	1.9	0.10	CaO-normalized Ds[c]
Element Paramaterizations					
CaO: $32.44 \times X_{CaO}^{(-0.89)}$ ($R^2 = 0.99$)[c]					
Al_2O_3: $0.87 - 0.045\ X_{Al2O3}$ ($R^2 = 0.95$)[c]					
Zr: $0.446 \times e^{(0.159 \times Al2O3)}$ ($R^2 = 0.87$)[c]					

[a] Calculated based on 8-fold ionic radii, although cations are in 12-fold coordination.
[b] Free parameter in regression.
[c] Regressions to data from Corgne and Wood (2002) and Hirose et al. (2004).

5.1.2. *Ca-Perovskite*

Ca-perovskite (CaPv) may have been an important crystallizing phase during solidification of a deep magma ocean (Presnall et al., 1998). At the pressure conditions of our experiments, CaPv is observed only in the subsolidus. However, recent experiments indicate that CaPv is stable within the crystallization interval at higher pressures (e.g., >30 GPa), beginning to crystallize at a similar temperature as FP (Ito et al., 2004). Recent experimental investigations of element partitioning between CaPv and melt have provided important new data (Corgne and Wood, 2002; Hirose et al., 2004).

CaPv crystallizes in an ideal, cubic perovskite structure with space group Pm3m. There are two crystallographic sites into which elements partition. An octahedral site occupied primarily by Si^{4+}, and a large, twelve-fold site occupied primarily by Ca^{2+}. Trace cations mix primarily into the large site. A fundamental difficulty in CaPv-melt partitioning experiments is that CaPv does not crystallize near the liquidus of model mantle peridotite compositions at maximum pressures typical in a multi-anvil cell (e.g., ~25 GPa). To achieve saturation in CaPv, the liquid compositions must be moved from normal peridotitic compositions toward Ca-rich, komatiitic or picritic compositions. There are considerable differences among liquid compositions in the studies of Corgne et al. (2002) and Hirose et al. (2004). Especially notable are variations in CaO and Al_2O_3 contents, which range from ~6.5 to 21 wt.% and 1.5 to 16 wt.%, respectively. We note that D^{Ca} and D^{Al} are correlated with melt CaO and Al_2O_3 contents, respectively, and the parameterizations given in Table 7 are used in crystallization models presented below.

Figure 6 shows reported partition coefficients for trivalent cations as a function of ionic radius for CaPv. Note that ionic radii for eightfold coordination have been used in the absence of information about radii in twelve-fold coordination. The three experiments shown exhibit similar partitioning behavior as a function of ionic radius, but have distinctly different absolute values of D that can be related to the CaO content of the melt. We fit a lattice-strain model to the partitioning data after the Ds from each experiment were normalized to the CaO content of the melt. The result is shown in Figure 6 and regression parameters are given in Table 7. An overall good fit to the data is achieved with a Young's modulus of 312 GPa and an ideal ionic radius of 1.05. Although this model is provi-

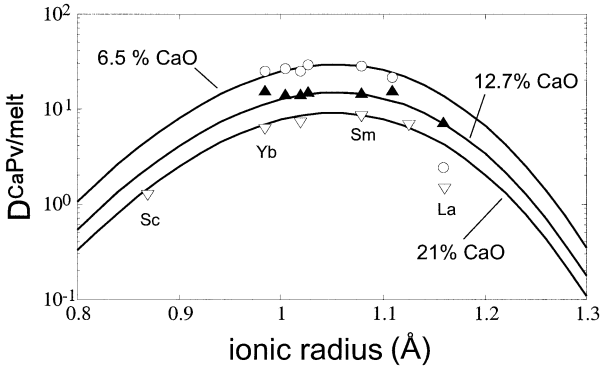

Fig. 6. Partition coefficients for trivalent cations in 1twofold coordination as a function of ionic radius (Å) for CaPv. Open circles are data from Corgne and Wood (2002), experiment #S2738. Solid triangles are data from Hirose et al. (2004), experiment #50. Open inverted triangles are data from Hirose et al. (2003), experiment #113. Ionic radii are from (Shannon, 1976). Solid curves are regressions of the lattice-strain equation to all partitioning data after normalization to CaO content in the melt (see text and Table 7).

sional, with CaO content in the melt as a proxy for melt composition effects, we note that the fitted r_o and Young's modulus are in general agreement with values obtained for CaPv in the lattice strain models of Corgne and Wood (2002). In the crystallization models presented below, we use this lattice strain model to predict D values for trivalent cations in CaPv as a function of melt CaO content.

There is not enough data available to fit a lattice-strain model to tetravalent cations like Hf and Zr that most likely also mix into the large site in CaPv, but these elements are important in geochemical modeling presented below. However, data from Corgne and Wood (2002) and Hirose et al. (2004) make a preliminary, empirical partitioning model possible. Zr apparently has a dependence on melt Al_2O_3 content, and an exponential fit to D^{Zr} versus melt Al_2O_3 is given in Table 7 and used in the crystallization models. Due to their nearly identical ionic radii, we assume that Hf has the same partition coefficient as Zr in CaPv, as is nominally the case for MgPv. This assumption is generally vindicated by the partitioning results of Corgne and Wood (2002). We note that the models presented below are not sensitive to the parameterized Ds for Hf and Zr within a factor of two.

6. GEOCHEMICAL MODELS OF CRYSTAL DIFFERENTIATION

Geochemical models for crystal differentiation in a deep magma ocean are inherently non-unique because assumptions are required about the bulk compositions of mantle reservoirs. To start, one must know the composition of the bulk-silicate Earth (BSE) (i.e., bulk Earth composition minus the core). The compositions of bulk Earth and, therefore, BSE cannot be directly determined because most of the Earth is not sampled and the bulk composition of accretionary materials cannot be uniquely defined. Next, one must know the composition of the convecting mantle. Convecting mantle (CM) is here defined as that portion of the mantle that has been convectively stirred since the mantle crystallized, or in other terms, since an early postaccretionary state. In this definition we assume implicitly that the 660 km seismic discontinuity is due to the dissociation of ringwoodite to MgPv + FP in a convecting mantle of essentially constant composition, and that the slightly negative Clapyron slope of this reaction has not been an effective impedance to mantle flow over Earth history (see Kennett and van der Hilst 1998) and Helffrich and Wood (2001) for discussions of this topic).

The CM could have essentially the same bulk composition as the BSE, at least for major elements, if no crystal fractionation ever occurred or if the entire mantle has been effectively remixed since the Hadean. Conversely, if a deep layer of early crystalline differentiates has remained isolated from convection due to rheologic stability, then the composition of the CM could be representative of a residual, differentiated liquid after crystal fractionation. Models for BSE and CM are both typically tied to primitive samples from the uppermost mantle, a fact that can potentially create circularity in geochemical arguments. Clearly, geochemical crystallization models are only meaningful if model compositions for BSE and CM are representative of actual chemical reservoirs.

We use two approaches to test for geochemical signals of crystal differentiation in a deep magma ocean. First, we use major element mass balance among a set of model BSE, CM, and deep mantle mineral compositions to explore and discriminate among a discrete set of possible model solutions. The mass balance approach suffers from a lack of absolute knowledge regarding reservoir compositions and because we use a set of constant mineral compositions, which effectively means an artificially changing $D^{min/melt}$ regardless of the CM composition (i.e., residual melt).

Second, we use experimentally determined mineral/melt partition coefficients to track changes in major and trace refractory lithophile element ratios in the residual melt as a function of degree of crystal fractionation, and make comparisons with model chondrite-normalized CM compositions (e.g., Kato et al., 1988; McFarlane et al., 1994). This approach is superior to mass balance in that it rests on the robust assumption that refractory lithophile element ratios were present initially in chondritic proportions in the BSE. However, a weakness in this approach is that partition coefficients are held constant in the models, even though they are likely to change with pressure, temperature and melt composition to some as yet undetermined degree. At present phase equilibrium data for crystallization of peridotite melt at lower mantle conditions are extremely limited and models simply cannot be constrained more fully.

6.1. Model Bulk Silicate Earth and Convecting Mantle

6.1.1. Bulk Silicate Earth (BSE)

In one class of BSE models (CI-BSE) it is postulated that bulk Earth has the composition of primitive, CI chondrite meteorites, and BSE is derived by difference after stripping away an Fe-Ni core constituting some 30% of Earth's mass, as well as some volatile elements (e.g., Taylor and McLennan, 1985). Beyond the fact that CI-chondrites are compositionally akin to the solar photosphere and therefore approximate primitive nebular composition, there is no a priori reason that bulk Earth must share that pedigree. In all likelihood, most of

Earth's mass accreted from an array of large objects, each with its own unique accretion and differentiation history. The provenance of these objects may have spanned as much as several A.U. (Wetherill, 1994), and little is known about heliocentric compositional gradients in the early nebula, especially for volatile elements. It is unlikely that bulk Earth composition can be reconstructed from any particular class of meteorite compositions (see O'Neill and Palme, 1998).

In a second class of peridotite-based BSE models (PB-BSE), correlations among refractory, lithophile major element ratios in chondritic meteorites and selected sets of primitive peridotites from the upper mantle have been used to infer that BSE has near-chondritic relative abundances of lithophile elements that are more refractory than Mg and Si in the solar nebula (e.g., Allegre et al., 1995; Hart and Zindler, 1986; McDonough and Sun, 1995; O'Neill and Palme, 1998; Wanke et al., 1984). In terms of major elements, the primary difference between the CI-BSE and PB-BSE models is in the Si content. In the CI-BSE models all refractory lithophile element ratios are chondritic, including Mg/Si, and the Si content of CI-BSE is considerably higher than in PB-BSE. The Si content in PB-BSE models is lower because the Mg/Si ratio of primitive peridotite from the upper mantle is decidedly super-chondritic. However, in PB-BSE models other refractory element ratios (e.g., Ca/Al, Ca/Ti, Al/Ti, Ca/Sc, Sc/Yb) are generally considered to be near-chondritic. The observation that many refractory element ratio trends indicate close to chondritic ratios in select sets of primitive mantle rocks, has led to the explicit assumption that primitive upper mantle, or CM, has the same composition as the BSE (Wanke et al., 1984; Hart and Zindler, 1986; Allegre et al., 1995; McDonough and Sun, 1995; O'Neill and Palme, 1998). To obtain a working major element model of PB-BSE composition, we calculated averages for this entire group, as well as a subset of the group that retains chondritic refractory element ratios for all major elements except Mg/Si (e.g., models of Hart and Zindler 1986 and Allegre et al. 1995), see Table 9).

6.1.2. Convecting Mantle (CM)

For purposes of trying to deduce a signal of early mantle differentiation, the debate centers on whether or not CM actually retains all refractory lithophile element ratios in strictly chondritic proportions. If the answer is yes, a severe constraint is placed on magma ocean differentiation models because crystallization cannot have perturbed these ratios one from another.

Some model primitive upper mantle compositions have previously been constructed without a presumption of chondritic refractory element ratios for primitive mantle. These are based on direct sampling of peridotites and their melting derivatives. Models have been based on primitive peridotite compositions (e.g., Jagoutz et al., 1979) and this study), mixtures of depleted peridotite and basalt ('pyrolite') (e.g., Ringwood, 1979), and melt extraction trends in residual peridotites (Walter, 2003). As a group, these various rock-based modeling techniques produce a consistent major element composition for primitive upper mantle. To obtain a working major element model of CM composition, we calculated averages for this entire group, as well as a subset of the group comprised only of averaged primitive peridotite compositions (e.g., data from Jagoutz et al. 1979 and this study). Model CM compositions are given in Tables 8 and 9 and element ratios shown on Figure 7. The model CM compositions calculated here have non-chondritic refractory major element ratios.

The Mg/Si of the upper mantle is undeniably superchondritic, but there are mitigating circumstances. Si is considered to be somewhat more volatile in a hot nebula gas, so a cosmochemical fractionation is a possibility (Ringwood, 1979; Wanke et al., 1984; Jones, 1996). Further complicating matters is the predilection of Si for Fe metal under conditions that may have been achieved during core formation (Ringwood, 1979; Gessman et al., 2001). Ratios of the more highly refractory elements (Ca/Al, Ca/Ti, Al/Ti, and to a lesser extent Al/Mg) should be cosmochemically more robust, and none of these elements is known to partition to any significant extent into core-forming metal. Al/Mg is nominally subchondritic in model CM, but a chondritic ratio is not precluded due to variations in the ratio among the models. Al/Ti and Ca/Ti are nominally chondritic, but variation among models is large for Ti, as are uncertainties in the ratios. The Cal/Al ratio is apparently superchondritic in primitive upper mantle rocks. Variation of this ratio among the CM model compositions is relatively small, and the implication is that the CM has a differentiated composition. It has been suggested that elevated Ca/Al in upper mantle rocks is due to an indelible low-pressure melt extraction signature (e.g., Wanke et al., 1984; McDonough and Sun, 1995). However, variations in Ca/Al versus cpx/opx ratios (proxies for degree of melt extraction) in residual mantle peridotites are consistent with a superchondritic upper mantle source ratio (Walter, 2003). A high Ca/Al ratio is also implicated in the source regions of Proterozoic and Archean komatiites (Walter, 1998), necessitating very early mantle differentiation.

6.1.3. Trace Element Composition of Convecting Mantle

Models for the trace element composition of the BSE are based, as with major elements, on the robust assumption of chondritic relative refractory lithophile element ratios (e.g., McDonough and Sun, 1995). However, estimating the trace element composition of CM before continental crust formation is more problematic. We start by reevaluating the refractory lithophile trace element composition of primitive upper mantle rocks.

Table 8 gives an estimate of abundances of refractory lithophile trace elements in the CM based on a select set of xenolith and orogenic lherzolite samples from the literature. These samples of upper mantle lithosphere are typically late Proterozoic in age, and presumably represent nearly pristine upper mantle at that time (see Walter, 2003). Nearly all estimates of primitive upper mantle and BSE compositions have Mg#'s of ~89. In the data set constructed here, we included samples that have been analyzed for trace elements and have Mg#s within a window ranging from 88.5 to 89.6. We filtered the data set to exclude data that showed obvious enrichments in LILE and LREE due to secondary processes.

A list of chondrite-normalized, refractory major and trace element ratios of CM are given in Table 8, and are plotted in Figure 7. A further complication in estimating CM composition is that we are probing for a signal of mantle differentiation that predates continental crust formation. Incompatible elements

Table 8. Refractory lithophile element ratios in convecting mantle.

	Wt%	2SE[e]		CNR[f]	ave	+CC[g]	max	min
Major elements[a]								
Si	21.1	0.07		Mg/Si	1.21	1.20	1.21	1.19
Ti	0.10	0.02		Ca/Al	1.15	1.13	1.16	1.10
Al	1.93	0.15		Al/Mg	0.90	0.92	0.99	0.85
Mg	23.0	0.13		Al/Ti	1.03	0.98	1.18	0.77
Ca	2.34	0.12		Ca/Ti	1.18	1.10	1.32	0.88
				Al/Sc	0.90	0.91	1.01	0.82
Trace elements[b]				Ca/Sc	1.03	1.03	1.11	0.94
	n[c]	ppm[d]	2SE	Al/Yb	0.94	0.93	1.05	0.81
Zr	27	8.26	1.19	Ca/Yb	1.07	1.04	1.15	0.94
Y	27	3.7	0.32	Sc/Yb	1.04	1.02	1.10	0.94
La	19	0.26	0.10	Sm/Yb	0.86	0.91	1.08	0.76
Nd	9	0.81	0.15	Sm/Sc	0.82	0.90	1.04	0.76
Sm	20	0.3	0.04	Sm/Zr	0.94	0.93	1.20	0.72
Yb	20	0.38	0.02	Zr/Y	0.92	0.98	1.21	0.79
Lu	20	0.064	0.00	Lu/Hf	1.41	1.26	1.55	1.04
Hf	20	0.19	0.03	Sm/Nd	1.14	1.06	1.41	0.80
Sc	35	14.56	0.45	Ce/Ba[h]	0.90			

[a] Major element abundances of convecting mantle are based on averages of primitive mantle compositions from Jagoutz et al. (1979), Ringwood (1979), Walter (2003), and this study (average of 85 spinel lherzolite xenoliths and orogenic peridotites from the filtered data set of Walter (2003), and with Mg#'s between 88.0 and 89.6, yielding a composition of SiO_2 = 44.97, Al_2O_3 = 3.59, FeO = 8.31, MgO = 38.24, CaO = 3.28).

[b] Convecting mantle trace element abundances calculated from primitive spinel lherzolite and orogenic peridotite samples with Mg# between 88.5 and 89.6. Data sources: (Beccaluva et al., 2001; Bodinier et al., 1988; Bonatti et al., 1986; Frey et al., 1991; Frey et al., 1985; Heinrich and Besch, 1992; Nimz et al., 1995; Roden et al., 1988; Wiechert et al., 1997; Xu et al., 1998; Zangana et al., 1999).

[c] Number of primitive mantle samples.

[d] Parts per million.

[e] Two standard errors.

[f] CNR = CI-chondrite normalized data based on chondra data from McDonough and Sun (1995). Errors in major element ratios are two standard errors of the mean of ratios in model convecting mantle compositions. Errors in trace element ratios are calculated' from two standard errors of the mean elemental abundances.

[g] +CC: compositions after the addition of 0.7% continental crust with compositions from http://earthref.org/GERM/index.html?main.htm

[h] Estimate based on OIB compositions reported in Halliday et al. (1995).

Table 9. Crystal differentiation mass balance calculations.

	BSE[a]			*CM*[b]		*LMP*[c]			*UMP*[d]		
	CI	BSE1	BSE2	CM1	CM2	MgPv	CaPv	FP	Maj	Olp	
SiO_2	49.9	45.72	46.04	45.17	45.21	54.9	51.0	0.2	52.2	43.9	
Al_2O_3	3.65	4.30	4.08	3.65	3.84	3.7	2.8	1.2	10.5	0.1	
FeO	8.0	7.77	7.52	8.09	8.07	4.3	3.0	9.9	2.5	7.0	
MgO	35.15	37.37	37.78	38.15	38.11	35.6	3.0	86	31	49.9	
CaO	2.9	3.46	3.22	3.27	3.40	0.8	38.0	0.1	4	0.1	
Solutions[e]											SSD[f]
MB1	1.0	—	—	1.0482	—	0.0480	−0.0157	−0.0809	—	—	0.11
MB2	—	1.0	—	0.9589	—	0.0397	0.0077	−0.0063	—	—	0.44
MB3	—	1.0	—	—	0.9669	0.0368	0.0039	−0.0076	—	—	0.23
MB4	—	1.0	—	0.9194	—	0.0690	0.0116	—	—	—	0.46
MB5	—	—	1.0	0.8648	—	0.1218	0.0077	0.0057	—	—	0.21
MB6	—	—	1.0	—	0.8697	0.1210	0.0044	0.0049	—	—	0.08
MB7	—	—	1.0	0.8820	—	—	—	—	0.0961	0.0219	0.04

[a] Bulk silicate Earth models (BSE). CI = model chondrite of Taylor and McLennan (1985); BSEI = average of Wanke (1984), Hart and Zindler (1986), Allegre et al. (1995), McDonough and Sun (1995), and O'Neill and Palme (1998). BSE2 = average of Hart and Zindler (1986) and Allegre et al. (1995).

[b] Convecting mantle models (CM). CMI = average convecting mantle as calculated in Table 8. CM2 = average of Jagoutz (1979) and this study.

[c] Lower Mantle Phases (LMP). MgPv = average composition of Mg-perovskite, this study. CaPv = composition of Ca-perovskite estimated from experimental data of Corgne and Wood (2002) and Hirose et al. (2004), with CaO and Al_2O_3 calculated from equations in Table 7 for a melt with 4% Al_2O_3 and 4% CaO. FP = ferropericlase composition from experiment #62, this study.

[d] Upper Mantle Phases (UMP). Majorite composition estimated from this study, and olivine polymorph (Olp) composition estimated to crystallize from ultramafic melt.

[e] Linear least squares solutions to mass balance equation, BSE = CM + MgPv + CaPv + FP.

[f] SSD = sum of the squared deviations.

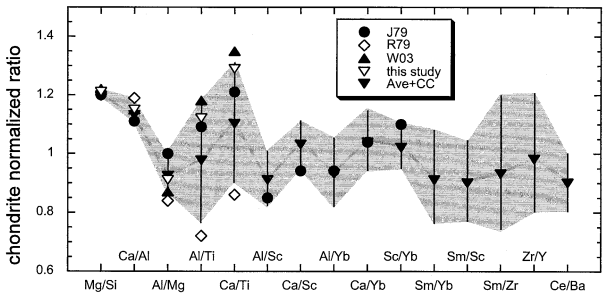

Fig. 7. Abundances of chondrite-normalized refractory lithophile elements in model convecting mantle compositions. J79 = Jagoutz et al. (1979); R79 = Ringwood (1979); W03 = Walter (2003). The model convecting mantle composition from this study is as described in Table 8. Ave + CC = the average convecting mantle plus a continental crust component (Table 8). Error bars are from estimated standard errors (Table 8). The shaded region is based on error bars, and the thick shaded line connects Ave + CC.

concentrate in the crust, and even though this reservoir constitutes a small relative mass (~0.7% of silicate Earth), it can have a considerable effect on element abundances in the mantle. For this reason, we have added back a continental crust component to the estimated CM composition (Table 8). The composition of the continental crust was taken as the average of values in the GERM database (http://earthref.org/GERM/index.html?main.htm). Figure 7 illustrates that, major element ratios aside, a relatively large suite of ratios remain within ~10–20% of chondritic in the CM. Notably absent from this group are ratios involving highly incompatible elements. The abundances of highly incompatible elements in natural peridotite are not well constrained, as they are much more susceptible than relatively compatible elements to small-scale melt-related processes. However, Ce/Ba has been shown to be remarkably constant in ocean island basalts at $\sim 0.9 \pm 0.2 \times$ CI chondritic (Halliday et al., 1995), and we use this value as representative of CM.

6.2. Mass Balance Models

Mass balance among model BSE, CM, and combinations of deep mantle phases is made assuming that:

$$\text{BSE} = \text{CM} + (\text{MgPv, CaPv, FP}) \text{ or } (\text{majorite, olivine}) \quad (3)$$

We calculated two model BSE and two CM compositions (Table 9), to illustrate how subtle compositional differences can lead to considerable differences in mass balance solutions. Mass balance is calculated assuming various combinations of deep mantle phases (e.g., majorite, MgPv, CaPv, FP, olivine polymorph). Given the inherent non-uniqueness of the mass balance approach the exercise is to be regarded as heuristic.

Solutions starting with CI-BSE are unrealistic because they require large amounts of negative components (e.g., FP in MB1 of Table 9, or olivine polymorph in mass balance involving upper mantle phases). This indicates that CM is not a likely residue of crystal differentiation starting from CI-BSE, and that the superchondritic Mg/Si in the upper mantle may be a primary feature of the mantle. Either accretionary materials were depleted in Si relative to Mg in which case bulk Earth is Si depleted, or Si was preferentially sequestered into Earth's core in which case only BSE is silica depleted (e.g., Ringwood, 1979; Allegre et al., 1995).

Mass balance that incorporates model BSE1 and lower mantle phases (MB2 and MB3 in Table 9) also yield solutions requiring negative amounts of FP. Eliminating FP from the lower mantle assemblage (MB4) produces a 'successful' solution, with ~8% removal of MgPv and CaPv in the proportion of 85:15. Mass balance that incorporates model BSE2 and lower mantle phases (MB5 and MB6 in Table 9) also yield 'successful solutions', in that all lower mantle minerals have positive coefficients. Mass balance indicates that model CM compositions can be derived by removing 13–14% of lower mantle phases, with the crystal assemblage dominated by MgPv (90–93%) and with 3–6% each of CaPv and FP.

A successful solution is also obtained for removal of ~12% of a combination of majorite and olivine polymorph (e.g., ringwoodite). These phases could crystallize together at depths corresponding to the mantle transition zone. However, it is difficult to envision how an isolated upper mantle layer rich in majorite could have been preserved in a convecting mantle. Further, we will show that models incorporating a predominant amount of majorite fractionation are limited to less than 5% crystal fractionation.

The gross failure of mass balance in providing realistic solutions for a CI-BSE provides further evidence against a CI chondrite bulk silicate Earth model. Successful solutions involving PB-BSE and CM are generally consistent with phase relations in that they indicate a crystal component dominated by MgPv (~90%) with subsidiary CaPv + FP (~10%) and that ~10–15% crystal fractionation can be accommodated from a major element perspective. To further test the plausibility of crystal differentiation in a magma ocean, we now use the $D^{min/melt}$ approach to examine how removal of deep mantle phases would be expected to fractionate a large suite of refractory lithophile element ratios.

6.3. The $D^{min/melt}$ Approach

In this approach we track changes in initially chondritic refractory lithophile element ratios as a function of degree of crystallization. We use the equation for perfect fractional crystallization:

$$C_i^l = C_i^{0,l} f^{\overline{D_i}-1} \quad (4)$$

where $C_i^{0,l}$ is the concentration of element i in the parent liquid, f is the weight proportion of residual liquid, and $\overline{D_i}$ is the bulk partition coefficient:

$$\overline{D_i} = \sum_\alpha D_i^{\alpha/l} X^\alpha \quad (5)$$

where $D_i^{\alpha/l}$ is the partition coefficient for element i between mineral α and liquid, and X^α is the weight fraction of the crystallizing mineral (e.g., Allegre and Minster, 1978). In principle, the style of crystallization could have ranged from perfect fractional to equilibrium crystallization. Perfect fractional crystallization produces the most extreme fractionations, but we note that the results presented below are not sensitive to the

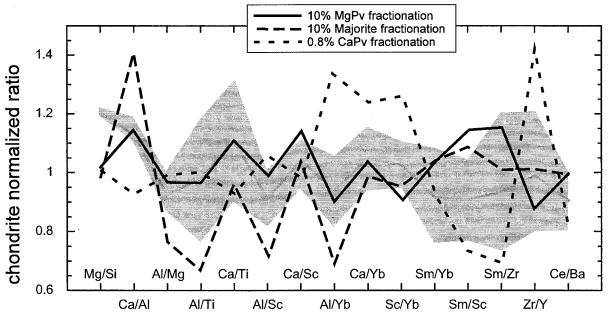

Fig. 8. Fractionation of refractory lithophile element ratios in residual magma after monomineralic removal of 10% MgPv (solid line), 10% majorite (long-dashed line) and 0.8% CaPv (short-dashed line), from a magma ocean with initially chondritic relative ratios. The shaded region is the chondrite-normalized element ratios in model convecting mantle from Figure 7. Major element partition coefficients (Ds) for majorite and MgPv are based on averages from Table 5. Trivalent trace element Ds for majorite are calculated from the lattice strain model with Young's modulus of 352 GPa, and for MgPv are calculated from the model with Young's modulus of 301 GPa (Table 6). Zr and Hf in majorite and MgPv are averages of measured values in Table 5. Ds for trivalent cations in CaPv are calculated from the lattice strain model in Table 7 based on a melt with 4% CaO. Ds for Al_2O_3, CaO, and Zr are based on parameterizations in Table 7 assuming a melt with 4% Al_2O_3 and 4% CaO. We assume $D_{Hf} = D_{Zr}$. Ds for Si and Mg in CaPv are based on measured values in Corgne and Wood (2002) and Hirose et al. (2004). D^{Ba} is estimated to be 0.2 in CaPv based on experiments of Hirose et al. (2004).

choice of the expression for quantifying element behavior during crystallization.

6.3.1. *Mono-mineralic fractionation*

Figure 8 shows how refractory lithophile element ratios fractionate during mono-mineralic, perfect fractional crystallization of MgPv, majorite, and CaPv. While it may be unlikely that any single phase would have become fractionated in isolation, Figure 8 illustrates the leverage that each mineral has on various element ratios. First, notice that MgPv does not have a particularly strong leverage on any ratio. Indeed, 10% fractionation of MgPv, which recaptures the Ca/Al ratio of model CM, produces fractionations in other ratios that are generally within the bounds of CM. We will show below (section 7.1), however, that the Hf-Nd isotopic systematics of modern oceanic volcanic rocks tightly constrain early removal of pure MgPv to something less than ~5%.

In contrast to MgPv, 10% removal of majorite produces large fractionations in ratios such as Ca/Al, Al/Mg, Ca/Ti, Al/Sc, and Al/Yb. We estimate the maximum amount of majorite fractionation that can be accommodated by the CM composition to be less than ~4%.

CaPv exerts extreme leverage on many element ratios and even less than 1% removal from the liquid would fractionate a number of ratios to values well outside the model CM composition. An intriguing feature of CaPv is that it produces fractionations in nearly every ratio that are antithetical to fractionation produced by MgPv. This occurs because in MgPv, the ideal eightfold site radius is closer to Mg^{2+} (~0.85 Å), but in CaPv the twelve-fold site radius is larger, closer to Ca^{2+} (~1.05Å). Thus, in MgPv compatibility decreases systematically from the HREE to the LREE because all the REE have ionic radii larger than the ideal site radius. Conversely, in CaPv the middle REE span the ideal site radius and both the HREE and LREE are more incompatible. Also, the REE are more compatible than Zr in CaPv, but are less compatible in MgPv. We show below that this relationship has important implications for elemental fractionations produced by crystallizing mixtures of deep mantle phases.

6.3.2. *Multi-mineralic fractionation*

Phase relations and mass balance indicate that crystallization in a deep magma ocean would have involved a crystalline assemblage dominated by MgPv with lesser amounts of CaPv and FP, especially during intermediate to later stages of fractional crystallization, or during melt expulsion from an aggregate formed by a high degree of equilibrium crystallization. Liquidus phase relations for fertile peridotite in the deeper parts of the lower mantle are as yet unknown, but initial results at pressures of ~30 to 33 GPa show that MgPv is the liquidus phase followed down temperature by FP and CaPv (Ito et al., 2004). Most importantly, these results indicate that as pressure increases, CaPv approaches the liquidus and crystallizes in small amounts together with FP. At present, the exact proportions of phases that would crystallize in the deep mantle cannot be deduced with certainty, and phase relations are expected to be pressure-, temperature- and composition-dependant. But in any case, we expect the crystallizing assemblage to be dominated by MgPv.

Figure 9 illustrates how various mixtures of deep mantle phases fractionate refractory lithophile element ratios. First, consider a crystalline mixture composed of 85% MgPv and 15% CaPv, as indicated by mass balance calculation MB4 in Table 9. Removal of such a mixture would produce extreme fractionations in several element ratios, most notably Al/Yb, Ca/Yb and Sc/Yb. CaPv has a large effect on the Ca/Al ratio opposite to MgPv, and for an 85:15 mix the Ca/Al ratio actually decreases in the residual melt. To produce an increase in the Ca/Al ratio in the melt in our models, the amount of CaPv in the crystallizing assemblage is limited to ~12%. If CaPv is reduced to just 5% of the crystallizing mix, then Al/Yb, Ca/Yb and Sc/Yb deviate substantially from the CM composition for an amount of crystallization (15%) that produces a match for the Ca/Al ratio.

Next, consider models for removal of deep mantle minerals in proportions that are more commensurate with solutions to mass balance calculations MB5 and MB6. Figure 9b illustrates, for example, that removal of 13% of an assemblage comprised of MgPv, CaPv and FP in the proportions 93:3:4 produces element ratios that remain generally consistent with those in the CM. Again, the total amount of fractionation (13%) was determined such that the Ca/Al ratio of the CM was matched exactly by that in the residual liquid, and in doing so there is a remarkable agreement in the pattern of fractionation and the CM pattern. We also note that this result is not particularly sensitive to the choice of lattice strain model to our data for trivalent cations (Fig. 9b).

There are numerous crystallization models that can be developed and those presented here are not uniquely defined. We hasten to point out that partition coefficients for many elements

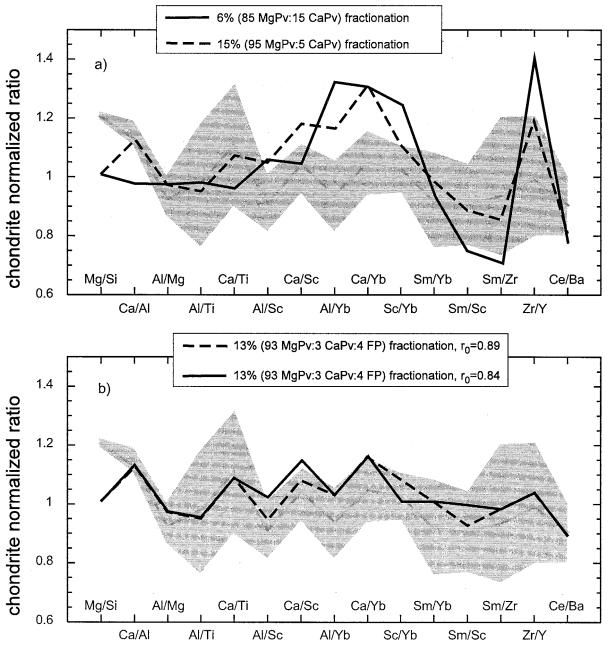

Fig. 9. Fractionation of refractory lithophile element ratios in residual magma after polymineralic removal of deep mantle phases from a magma ocean with initially chondritic relative ratios. Chondrite-normalized element ratios in model convecting mantle are shown by the shaded region. a) Removal of 6% of the assemblage 85MgPv:15CaPv (solid line) and 15% of the assemblage 90MgPv:5CaPv:5FP (dashed line). b) Removal of 13% of the assemblage 93MgPv:3CaPv:4FP using different lattice strain models for trivalent cations in MgPv from Table 6 (r_0 = 0.84 Å, E = 301 GPa, solid line; r_0 = 0.89 Å, E = 378 GPa, dashed line). Other element Ds as in Figure 8.

in CaPv are very sensitive to melt compositional parameters, compositional dependencies that are just now beginning to be explored in a systematic way. The results presented here are for a specific model liquid composition with 4 wt.% CaO and 4 wt.% Al_2O_3, but the residual liquid is expected to continuously change in composition as phases are removed (i.e., a high pressure liquid line of descent). For example, increasing the melt CaO content reduces significantly the absolute D values for many trivalent elements in CaPv, thereby reducing its leverage on element fractionations and permitting a somewhat larger abundance in the crystallizing assemblage. Element partition coefficients in MgPv are also likely to show pressure, temperature and compositional dependence, so the models produced here must be viewed as provisional. Given these caveats, geochemical models indicate the possibility that a deep mantle pile of crystalline differentiates (e.g., 93% Pv + 3% CaPv + 4% FP) constituting roughly 10 to 15% of the mantle can produce chemical fractionations that are generally consistent with the composition of model convecting mantle. Such a layer would be rich in Si, but depleted in Al and Fe relative to residual mantle. To survive subsequent convective stirring, this layer must have a sufficient rheological contrast with overlying material. Phase stability relations, let alone physical properties, of silicate and oxide phases in the deep lower mantle, especially the effects of composition and temperature on elastic properties, are not well enough known to predict accurately the stability of such a layer.

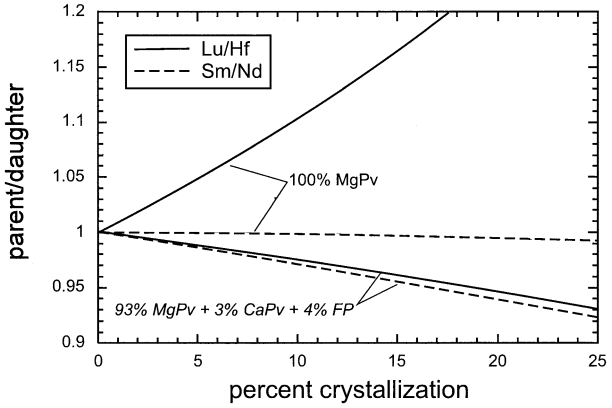

Fig. 10. Fractionation of chondrite normalized Sm/Nd and Lu/Hf ratios as a function of crystal fraction for fractional crystallization of pure MgPv and for a 93:3:4 mixture of MgPv, CaPv and FP. Model partition coefficients as in Figure 8. Solid lines show Lu/Hf fractionation and dashed lines Sm/Nd fractionation.

7. ISOTOPIC CONSTRAINTS ON EARLY CRYSTAL FRACTIONATION

Entertaining the plausible existence of a deep crystal pile, what effects might such a reservoir have on mantle isotopic evolution? Due to a lack of direct rock samples from the Hadean, the state of chemical differentiation in the earliest mantle is best constrained from radiogenic isotopes in younger rocks and minerals. The long lived $^{147}Sm \rightarrow {}^{143}Nd$ ($t_{1/2}$ = 106 Ga) and $^{176}Lu \rightarrow {}^{176}Hf$ ($t_{1/2}$ = 37 Ga) and the short lived $^{146}Sm \rightarrow {}^{142}Nd$ ($t_{1/2}$ = 103 Ma) isotope systems have been used extensively as probes of early mantle differentiation and crust formation (e.g., Galer and Goldstein, 1991; Harper and Jacobsen, 1992; Bowring and Housh, 1995; Albarede et al., 2000; Caro et al., 2003). Positive $\varepsilon 143_{Nd}$ and $\varepsilon 76_{Hf}$ (values that reflect time-integrated changes in parent/daughter ratios relative to growth in a chondritic reservoir) already in rocks from the earliest Archean have been interpreted to indicate differentiation in the Hadean mantle, most likely by early formation of a mafic protocrust or continental crust (e.g., Bowring and Housh, 1995; Vervoort and Blichert-Toft, 1999; Amelin et al., 2000). Recent high precision measurements of ^{142}Nd in Archean rocks yield distinctly positive values of $\varepsilon 142_{Nd}$ at ~3.75 Ga ago (Boyet et al., 2003; Caro et al., 2003). Modeling indicates the existence of a mantle reservoir with high Sm/Nd ('depleted') relative to chondrite as early as ~4.46 Ga ago (Caro et al., 2003). This mantle depletion indicates very early extraction of crustal material from convecting mantle. Interestingly, combined $\varepsilon 143_{Nd}$ and $\varepsilon 142_{Nd}$ systematics apparently are not easily reconciled by extraction of continental crust alone, implying another differentiation mechanism perhaps related to solidification of the Hadean magma ocean (Caro et al., 2003). Isotope systematics can place the tightest constraints on Sm/Nd and Lu/Hf ratios in the early mantle (e.g., Blichert-Toft and Albarede, 1997; Salters and White, 1998).

In Figure 10 we plot fractionation trends for Sm/Nd and Lu/Hf for crystal fractionation in a deep magma ocean. Extraction of pure MgPv generates a marked increase in Lu/Hf and a small decrease in Sm/Nd. CaPv has a high Lu/Hf ratio and exerts considerable leverage due to high absolute Ds for REE.

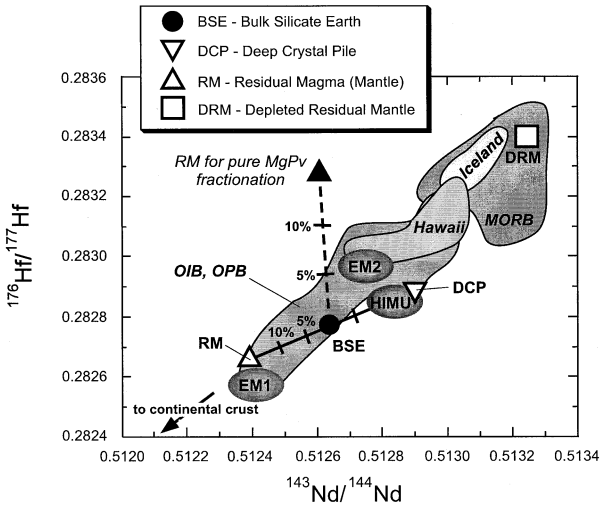

Fig. 11. The $^{176}Hf/^{177}Hf$ and $^{143}Nd/^{144}Nd$ isotopic compositions of modern, mantle derived volcanic rocks. The fields for midocean ridge basalt (MORB), ocean island basalt (OIB), ocean plateau basalts (OPB), Hawaii and Iceland, as well as the compositions of bulk silicate Earth (BSE), depleted residual mantle (DRM) and mantle isotopic components (EM1, EM2 and HIMU) are taken from Blichert-Toft and Albarede (1997) and Salters and White (1998). Two models are shown for the effect of early removal and isolation from the BSE of deep mantle phases in a Hadean magma ocean. The vertical dashed trend shows the model time-integrated modern isotopic compositions in the residual magma (convecting mantle) for removal of up to 15% of pure MgPv. The solid hatched line shows isotopic compositions in both the deep crystal pile (DCP) and residual magma (RM) for removal of up to 15% of an assemblage composed of 93% Mg-perovskite, 3% Ca-perovskite and 4% ferropericlase. In the models, isotopic growth occurs in a chondritic reservoir for the first 30 Ma. At 4.536 Ga ago Sm/Nd and Lu/Hf are fractionated relative to their initially chondritic values in the BSE based on fractionation factors shown in Figure 10. Isotopic in-growth occurs in isolated DCP and RM reservoirs until the present. Values used in the calculations are $\lambda^{147}Sm = 6.54 \times 10^{-12}$ yr and $\lambda^{176}Lu = 1.93 \times 10^{-11}$ yr, $\left(^{147}Sm/^{144}Nd\right)_{tp}^{CHUR} = 0.1967$, $\left(^{143}Nd/^{144}Nd\right)_{tp}^{CHUR} = 0.512638$, $\left(^{176}Lu/^{176}Hf\right)_{tp}^{CHUR} = 0.0332$, and $\left(^{176}Hf/^{177}Hf\right)_{tp}^{CHUR} = 0.282772$.

When CaPv comprises just 3% of the crystal assemblage, and if the partition coefficients for CaPv calculated for 4% CaO in the melt are used, both the Lu/Hf and Sm/Nd ratios decrease similarly from an initially chondritic value. The Lu/Hf ratio is especially sensitive to model parameters. As the amount of CaPv in the crystal assemblage decreases, or if the CaO content of the melt increases, the Lu/Hf ratio decreases at a slower rate or eventually increases.

Figure 11 shows $^{143}Nd/^{144}Nd$ versus $^{176}Hf/^{177}Hf$ for modern oceanic volcanic rocks. Isotopic compositions form a relatively tight array that passes through an estimated model chondritic BSE reservoir (e.g., Blichert-Toft and Albarede, 1997). Correlated positive and negative deviations from BSE are interpreted to reflect mantle components that are both radiogenic (e.g., the depleted MORB source) and unradiogenic (e.g., the enriched EMI OIB source) relative to BSE. Early fractionation of Sm/Nd and Lu/Hf, such as might have occurred by crystal fractionation in a magma ocean, is restricted to produce a residual mantle reservoir (e.g., source of volcanics) that also lies within the volcanic array. Figure 11 shows that early fractionation of pure MgPv would generate a residual magma (CM) reservoir with elevated $^{176}Hf/^{177}Hf$ relative to BSE with a negligible decrease in $^{143}Nd/^{144}Nd$. No more than ~5% removal of MgPv can be tolerated before isotopic compositions of subsequently formed reservoirs (e.g., depleted MORB mantle or OIB sources) would lie outside the volcanic array. This observation has been used as an argument against crystal fractionation in a magma ocean (e.g., Salter and White, 1998).

Figure 11 also shows how the isotopic compositions of the residual magma (CM) and deep crystal pile would have evolved for removal of an assemblage comprised of 93% Pv + 3% CaPv + 4% FP. As shown in Figure 10, both Sm/Nd and Lu/Hf decrease similarly in the residual magma. Model isotopic compositions for the residual magma form an array that parallels the volcanic array, and lie internal to the array for up to ~15% total crystal fractionation. Indeed, we note that 15% crystal fractionation produces isotopic reservoirs that closely approximate EM1 (residual magma or CM) and HIMU (deep crystal pile), at least in Hf-Nd isotope space. Thus, as is the case for other refractory element ratios, removal of 10 to 15% of a deep mantle crystal assemblage produces Sm/Nd and Lu/Hf fractionations that are tolerable on isotopic grounds.

8. CONCLUDING REMARKS ON EARLY EARTH DIFFERENTIATION

Consider a time within the first few tens of million of years of accretion when the proto-Earth grew large enough for its silicate mantle to thicken to the point where its lower reaches penetrated the perovskite stability field. Stochastic accretion models suggest that it is most likely that the size-threshold for perovskite stability would have been achieved as a consequence of a giant impact between proto-Earth and a large bolide (Chambers and Wetherill, 1998). The energy deposited in such a massive impact could have rendered the silicate largely molten (Tonks and Melosh, 1993), making possible the removal of deep mantle perovskite and oxide phases by crystal fractionation or melt expulsion. Any later large impact that heated enough to melt at depths corresponding to perovskite stability could have induced a subsequent stage of ultra-high pressure fractionation. As Earth accreted to its final size and subsequently cooled, vigorous stirring of a mushy mantle may have re-worked and homogenized nascent layering. A proto-crystal pile of deep mantle phases may have been eroding at various rates since primordial crystallization. We conjecture that some amount of dense crystalline fractionate might have remained rheologically stable at the base of the mantle. Our geochemical and isotopic models permit moderate amounts (e.g., 10 to 15%) of an isolated ultra-high pressure crystal fraction predominated by Mg-perovskite and with a minor but important amount of Ca-perovskite. Models indicate that the elemental and isotopic characteristics of the residual magma would be generally consistent with those observed in primitive upper mantle rocks. However, these models must be viewed as provisional given the uncertainties in model parameters such as the compositions of mantle reservoirs and the as yet undetermined dependence of major and trace element partitioning on pressure, temperature and composition.

Acknowledgments—M. Walter acknowledges support from the Lawrence Berkeley and Lawrence Livermore National Laboratories during

preparation of this manuscript. The initial experimentation by RGT and DJF in Bayreuth was funded by the EU-TMR Large Scale Facilities Programme (contract to D.C. Rubie). We thank J. Blundy, A. Corgne, T. Elliot, A. Halliday, K. Hirose, B. McDonough, D. Presnall, and B. Wood for discussions and access to submitted data. We thank W. van Westrenen and two anonymous reviewers for helpful comments that improved the manuscript.

REFERENCES

Agee C. B. and Walker D. (1988) Mass balance and phase density constraints on early differentiation of chondritic mantle. *Earth Planet Sci. Lett.* 90, 144–156.

Albarede F., Blichert-Toft J., Vervoort J. D., Gleason J. D., and Rosing M. (2000) Hf-Nd isotopic evidence for a transient dynamic regime in the early terrestrial mantle. *Nature* 404, 488–490.

Albarede F. and van der Hilst R. D. (1999) New mantle convection model may reconcile conflicting evidence. *EOS* 80, 535, 537-539.

Allegre C. J., and Minster J. F. (1978) Quantitative models of trace element behavior in magmatic processes. *Earth Planet Sci. Lett.* 38, 1–25.

Allegre C. J., Poirier J. P., Humbler E., and Hofmann A. W. (1995) The Chemical Composition of the Earth. *Earth Planet Sci. Lett.* 134, 515–526.

Amelin Y., Lee D.-C., and Halliday A. N. (2000) Early-middle Archean crustal evolution deduced from Lu-Hf and U-Pb isotopic studies of single zircon grains. *Geochim. Cosmochim. Acta* 64, 4205–4225.

Andrault D. (2003) Cationic substitution in $MgSiO_3$ perovskite. *Phys. Earth Planet. Int.* 136, 67–78.

Andrault D., Neuville D., Flank A. M., and Wang Y. (1998) Cation coordination sites in Al-$MgSiO_3$ perovskite. *Am. Mineral.* 83, 1045–1053.

Beccaluva L., Bianchini G., Coltorti M., Perkins W. T., Siena F., Vaccaro C., and Wilson M. (2001) Multistage evolution of the European lithospheric mantle: new evidence from Sardinia peridotite xenoliths. *Contrib. Mineral. Petrol.* 142, 284–297.

Benz W. and Cameron G. W. (1990) Terrestrial effects of the giant impact. In *Origin of the Earth* (ed. H. E. Newsom and J. H. Jones), pp. 61–67. Oxford University Press.

Blichert-Toft J., and Albarede F. (1997) The Lu-Hf isotope geochemistry of chondrites and the evolution of the mantle-crust system. *Earth Planet Sci. Lett.* 148, 243–258.

Blundy J., and Wood B. (2003) Partitioning of trace elements between crystals and melts. *Earth Planet Sci. Lett.* 210, 383–397.

Blundy J. D., and Wood B. J. (1994) Prediction of crystal-melt partition coefficients from elastic moduli. *Nature* 372, 452–454.

Bodinier J. D., Dupuy C., and Dostal J. (1988) Geochemistry and petrogenesis of Eastern Pyrenean peridotites. *Geochim. Cosmochim. Acta* 52, 2893–2907.

Bonatti E., Ottonello G., and Hamlyn P. R. (1986) Peridotites form the island of Zabargad (St. John), Red Sea: petrology and Geochemistry. *J. Geophys. Res.* 91(B1), 599–631.

Bowring S. A., and Housh T. (1995) The Earth's early evolution. *Science* 269, 1535–1540.

Boyet M., Blichert-Toft J., Rosing M., Storey M., Telouk P., and Albarede F. (2003) ^{142}Nd evidence for early Earth differentiation. *Earth Planet Sci. Lett.* 214, 427–442.

Canup R., and Asphaug E. (2001) Origin of the Moon in a giant impact near the end of Earth's formation. *Nature* 412, 708–712.

Caro G., Bourdon B., Birck J.-L., and Moorbath S. (2003) ^{146}Sm-^{142}Nd evidence from Isua metamorphosed sediments for early differentiation of the Earth's mantle. *Nature* 423, 428–432.

Chambers J. E., and Wetherill G. W. (1998) Making the terrestrial planets: N-body integrations of planetary embryos in three dimensions. *Icarus* 136, 304–327.

Corgne A., Allan N. L., and Wood B. J. (2003) Atomistic simulations of trace element incorporation into the large site of $MgSiO_3$ and $CaSiO_3$ perovskites. *Phys. Earth Planet. Int.* 139, 113–127.

Corgne A. and Wood B. J. (2002) $CaSiO_3$ and $CaTiO_3$ perovskite-melt partitioning of trace elements. Implications for gross mantle differentiation. *Geophys. Res. Lett.* 2001GL014398.

Corgne A. and Wood B. J. (2004) Trace element partitioning between majoritic garnet and silicate melt at 25 GPa. *Phys. Earth Planet. Int.* 143-144, 407-419.

Drake M. J., McFarlane E. A., Gasparik T., and Rubie D. C. (1993) Mg-perovskite/silicate melt and majorite garnet/silicate melt partition coefficients in the system CaO-MgO-SiO_2 at high temperatures and pressures. *J. Geophys. Res.* 98, 5427–5431.

Finger L. W. and Hazen R. M. (2000) Systematics of high-pressure silicate structures. In *High-Temperature and High Pressure Crystal Chemistry* (ed. R. M. Hazen and R. T. Downs), Vol. 41, pp. 123–156. The Mineralogical Society of America.

Frey F. A., Shimizu N., Leinbach A., Obata M., and Takazawa E. (1991) Compositional variations within the low layered zone of the Horoman Peridotite, Hokkaido, Japan: Constraints on models for melt-solid segtrgation. *J. Petrol.* (Special Lherzolites Issue) 211–227.

Frey F. A., Suen C. J., and Stockman H. W. (1985) The Ronda high temperature peridotite: Geochemistry and petrogenesis. *Geochim. Cosmochim. Acta* 49, 2469–2491.

Frost D. J., and Langenhorst F. (2002) The effect of Al_2O_3 on Fe-Mg partitioning between magnesiowustite and magnesium silicate perovskite. *Earth Planet Sci. Lett.* 199, 227–241.

Galer S. J. G., and Goldstein S. L. (1991) Early mantle differentiation and its thermal consequences. *Geochim. Cosmochim. Acta* 55, 227–239.

Gessman C. K., Wood B. J., Rubie D. C., and Kilburn M. R. (2001) Solubility of silicon in liquid metal at high pressure: implications for the composition of the Earth's core. *Earth Planet Sci. Lett.* 184, 367–376.

Halliday A. N., Lee D.-C., Tommasini S., Davies G. R., Paslick C. R., Fitton J. G., and James D. E. (1995) Incompatible trace elements in OIB and MORB and source enrichment in the sub-oceanic mantle. *Earth Planet Sci. Lett.* 133, 379–395.

Harper C. L., and Jacobsen S. B. (1992) Evidence from coupled ^{147}Sm-^{143}Nd and ^{146}Sm-^{142}Nd for very early (4.5 Ga) differentiation of the Earth's mantle. *Nature* 360, 728–732.

Hart S. R., and Zindler A. (1986) In search of a bulk-Earth composition. *Chem. Geol.* 57, 247–267.

Heinrich W., and Besch T. (1992) Thermal history of the upper mantle beneath a young back-arc extensional zone: ultramafic xenoliths from the San Luis potosì, Central Mexico. *Contrib. Mineral. Petrol.* 111, 126–142.

Helffrich G. R., and Wood B. J. (2001) The Earth's mantle. *Nature* 412, 501–507.

Hirose K., Shimizu N., Westrenen W. V., and Fei Y. (2004) Trace element partitioning in Earth's lower mantle and implications for geochemical consequences of partial melting at the core-mantle boundary. *Phys. Earth Planet. Int.* **6,** 249-260.

Horiuchi H., Ito E., and Weidener D. J. (1987) Perovskite-type $MgSiO_3$: Single-crystal X-ray diffraction study. *Am. Mineral.* 72, 357–360.

Ito E., Katsura T., Kubo A., and Walter M. (2004) Melting experiments of mantle materials under lower mantle conditions with implication to fractionation in magma ocean. *Phys. Earth Planet. Int.* 143-144, 397-406.

Jagoutz E., Palme H., Baddenhausen H., Blum K., Cendales K., Dreibus G., SPettel B., Lorenz V., and Wanke H. (1979) The abundances of major, minor and trace elements in the Earth's mantle as derived from primitive ultramafic nodules. *Proc. 10th Lunar Planet. Sci. Conf.*, 2031-2050.

Jeanloz R., and Williams Q. (1998) The core-mantle boundary region. In *Ultrahigh-Pressure Mineralogy* (ed. P. H. Ribbe), Reviews in Mineralogy Vol. 37, pp. 241–259. Mineralogical Society of America, Washington D.C., 2000.

Jones J. H. (1996) Chondrite models for the composition of the Earth's mantle and core. *Phil. Trans. Roy. Soc. Lond. A.* 354, 1481–1494.

Kato T., Ringwood A. E., and Irifune T. (1988) Experimental determination of element partitioning between silicate perovskites, garnets and liquids: constraints on early differentiation of the mantle. *Earth Planet. Sci. Lett.* 89, 123–145.

Kellogg L. H., Hager B. H., and Hilst R. D. v. d. (1999) Compositional stratification in the deep mantle. *Science* 283, 1881–1884.

Kennett B. L. N. and Hilst R. D. v. d. (1998) Seismic structure of the mantle: from subduction zone to craton. In *The Earth's Mantle: Composition, Structure and Evolution* (ed. I. Jackson), pp. 381–404. Cambridge University Press.

Lesher C., Pickering-Witter J., Baxter G., and Walter M. (2003) The dry mantle solidus at 5 GPa. *Am. Mineral.* 88, 1181–1189.

Lesher C. E., and Walker D. (1988) Cumulate maturation and melt migration in a temperature gradient. *J. Geophys. Res.* 93, 10295–10311.

Makishima A., and Nakamura E. (1997) Suppression of matrix effects in ICP-MS by high power operation of ICP: Application to precise determination of Rb, Sr, Y, Cs, Ba, REE, Pb, Th and U at ng g-1 levels in milligram silicate samples. *Geostand. News.* 21, 307–319.

McDonough W. F., and Sun S.-S. (1995) The composition of the Earth. *Chem. Geol.* 120, 223–253.

McFarlane E. A., Drake M. J., and Rubie D. C. (1994) Element partitioning between Mg-perovskite, magnesiowustite, and silicate melt at conditons of the Earth's mantle. *Geochim. Cosmochim. Acta* 58, 5161–5172.

Nakamura E., and Kushiro I. (1998) trace element diffusion in jadeite and diopside melts at high pressures abd its geochemical implications. *Geochim. Cosmochim. Acta* 62, 3151–3160.

Nakamura E., Suzuki T., Kobayashi K., Makishima A., and Akaogi M. (2001) Determination of trace element partitioning between majorite and silicate melt in the primitive mantle composition at pressure of 15 GPa. *Abstracts of Material Recycling in the Dynamic Earth, Misasa, Japan.* 148–149.

Nimz G. J., Cameron K. L., and Niemeyer S. (1995) Formation of mantle lithosphere beneath northern Mexico: Chemical and Sr-Nd-Pb isotopic systematics of peridotite xenolith from La Olivina. *J. Geophys. Res.* 100(B3), 4181–4196.

O'Neill H. S. C. and Palme H. (1998) Composition of the silicate Earth: Implications for accretion and core formation. In *The Earth's Mantle: Composition, Structure and Evolution* (ed. I. Jackson), pp. 3–126. Cambridge University Press.

Presnall D. C., and Walter M. J. (1993) Melting of Forsterite, Mg_2SiO_4, from 9.7 to 16.5 GPa. *J. Geophys. Res.* 98, 19,777–19,783.

Presnall D. C., Weng Y. H., Milholland C. S., and Walter M. J. (1998) Liquidus Phase Relations in the System MgO-$MgSiO_3$ at Pressures up to 25 Gpa—Constraints on Crystallization of a Molten Hadean Mantle. *Phys. Earth Planet. Int.* 107, 83–95.

Richmond N. C., and Brodholt J. P. (1998) Calculated role of aluminum in the incorporation of ferric iron into magnesium silicate perovskite. *Am. Mineral.* 83, 947–951.

Ringwood A. E. (1979) Origin of the Earth and Moon. Springer-Verlag, Berlin.

Roden M. F., Irving A. J., and Murthy V. R. (1988) Isotopic and trace element composition of the upper mantle beneath a young continental rift: Results from Kilbourne Hole, New Mexico. *Geochim. Cosmochim. Acta* 52, 461–473.

Salters V. J. M., and White W. M. (1998) Hf isotopic constraints on mantle evolution. *Chem. Geol.* 145, 447–460.

Shannon R. D. (1976) Revised effective ionic radii and systematic studies of interatomic distances in halides and chalcogenides. *Acta Crystal.* A32, 751–767.

Solomatov V. S. (2000) Fluid dynamics of a terrestrial magma ocean. In *Origin of the Earth and Moon* (ed. R. Canup and K. Righter), pp. 323–338. The University of Arizona Press.

Taylor S. R., and McLennan S. M. (1985) The Continental Crust: Its Composition and Evolution. Blackwell, Oxford.

Tonks W. B. and Melosh H. J. (1990) The physics of crystal settling and suspension in a turbulent magma ocean. In *Origin of the Earth* (ed. H. E. Newsom and J. H. Jones), pp. 151–174. Oxford University Press.

Tonks W. B., and Melosh H. J. (1993) Magma ocean formation due to giant impacts. *J. Geophys. Res.* 98, 5319–5333.

Trønnes R. G., and Frost D. J. (2002) Peridotite melting and mineral-melt partitioning of major and minor elements at 22-24.5 GPa. *Earth Planet. Sci. Lett.* 97, 117–131.

van der Hilst R. D., and Karason H. (1999) Compositional heterogeneity in the bottom 1000 kilometers of Earth's mantle: Toward a hybrid convection model. *Science* 283, 1885–1888.

van Keken P. E., Hauri E. H., and Ballentine C. J. (2002) Mantle mixing. The generation, preservation, and destruction of chemical heterogeneity *Ann. Rev. Earth Planet. Sci.* 30, 493–525.

van Westrenen W., Blundy J. D., and Wood B. J. (1999) Crystal-chemical controls on trace element partitioning between garnet and anhydrous silicate melt. *Am. Mineral.* 84, 838–847.

Vervoort J. D., and Blichert-Toft J. (1999) Evolution of the depleted mantle: Hf isotopic evidence from juvenile rocks through time. *Geochim. Cosmochim. Acta* 63, 533–556.

Walker D., and Agee C. (1989) Partitioning "equilibrium," temperature gradients, and constraints of Earth differentiation. *Earth Planet. Sci. Lett.* 96, 49–60.

Walter M. J. (1998) Melting of Garnet Peridotite and the Origin of Komatiite and Depleted Lithosphere. *J. Petrol.* 39, 29–60.

Walter M. (2003) Melt extraction and compositional variability in mantle lithosphere. In *The Mantle and Core* (ed. R. W. Carlson) Vol. 2. Treatise on Geochemistry, (eds. H. D. Holland and K. K. Turekian) pp 363-394. Elsevier-Pergamon, Oxford.

Walter M. J., Thibault Y., Wei K., and Luth R. W. (1995) Characterizing experimental pressure and temperature conditions in multi-anvil apparatus. *Can. J. Phys.* 73, 273–286.

Wanke H., Dreibus G., and Jagoutz E. (1984) Mantle chemistry and accretion history of the Earth. In *Archean Geochemistry* (ed. A. K. e. al), pp. 1–24. Springer-Verlag.

Wetherill G. W. (1994) Provenance of the terrestrial planets. *Geochim. Cosmochim. Acta* 58, 4513–4520.

Wiechert U., Ionov D. A., and Wedepohl K. H. (1997) Spinel peridotite xenoliths from the Atsagin-Dush volcano, Dariganga lava plateau, Mongolia: a record of partial melting and cryptic metasomatism in the upper mantle. *Contrib. Mineral. Petrol.* 126, 346–364.

Wood B. J., and Blundy J. D. (1997) A predicitve model for rare earth element partitioning between clinopyroxene and anhydrous silicate melt. *Contrib. Mineral. Petrol.* 129, 166–181.

Wood B. J., and Blundy J. D. (2001) The effect of cation charge on crystal-melt partitioning of trace elements. *Earth Planet. Sci. Lett.* 188, 59–71.

Xu Y., Menzies M. A., Vroon P., Mercier J., and Lin C. (1998) Texture-temperature-geochemistry relationships in the upper mantle as revealed from spinel peridotite xenoliths from Wangqing, NE China. *J. Petrol.* 39(3), 469–493.

Zangana N. A., Downes H., Thirlwall M. F., Marriner G. F., and Bea F. (1999) Geochemical variation in peridotite xenoliths and their constituent clinopyroxenes from Ray pic (French Massif Central): implications for the compositions of the shallow lithospheric mantle. *Chem. Geol.* 153, 11–35.